

# LYMAN $\alpha$ RADIATIVE TRANSFER WITH DUST: ESCAPE FRACTIONS FROM SIMULATED HIGH-REDSHIFT GALAXIES

PETER LAURSEN<sup>1</sup>, JESPER SOMMER-LARSEN<sup>3,1</sup> AND ANJA C. ANDERSEN<sup>1</sup>

*2nd draft*

## ABSTRACT

The Lyman  $\alpha$  emission line is an essential diagnostic tool for probing galaxy formation and evolution. Not only is it commonly the strongest observable line from high-redshift galaxies but from its shape detailed information about its host galaxy can be revealed. However, due to the scattering nature of Ly $\alpha$  photons increasing their path length in a non-trivial way, if dust is present in the galaxy the line may be severely suppressed and its shape altered. In order to interpret observations correctly, it is thus of crucial significance to know how much of the emitted light actually escapes the galaxy.

In the present work, using a combination of high-resolution cosmological hydro-simulations and an adaptively refinable Monte Carlo Ly $\alpha$  radiative transfer code including an advanced model of dust, the escape fractions  $f_{\text{esc}}$  of Ly $\alpha$  radiation from high-redshift ( $z = 3.6$ ) galaxies are calculated. In addition to the average escape fraction, the variation of  $f_{\text{esc}}$  in different directions and from different parts of the galaxies is investigated, as well as the effect on the emergent spectrum.

Escape fractions from a sample of simulated galaxies of representative physical properties are found to decrease for increasing galaxy virial mass  $M_{\text{vir}}$ , from  $f_{\text{esc}}$  approaching unity for  $M_{\text{vir}} \sim 10^9 M_{\odot}$  to  $f_{\text{esc}}$  less than 10% for  $M_{\text{vir}} \sim 10^{12} M_{\odot}$ . In spite of the dust being almost grey, it is found that the emergent spectrum is affected non-uniformly, with the escape fraction of photons close to the line center being much higher than of those in the wings, thus effectively narrowing the Ly $\alpha$  line.

*Subject headings:* galaxies: high-redshift — radiative transfer — dust — extinction — scattering — line: formation — line: profiles

## 1. INTRODUCTION

Many astrophysical and cosmological key questions depend upon precise measurements of the luminosities of distant galaxies; in particular, galactic star formation rates (SFRs) and histories, as well as luminosity functions (LFs), are crucially contingent on the amount of assumed luminosities. A fundamental problem in this context is naturally the question of how large a fraction of the emitted light actually escapes the galaxy. If an unknown fraction of the emitted light is absorbed, either by gas or by dust, the inferred quantity of interest clearly will be subject to large uncertainties or, at best, a lower limit.

The Ly $\alpha$  line, albeit notoriously challenging to interpret, is an extremely powerful probe of the high-redshift Universe. At  $z > 2.1$ , the cosmological redshift of Ly $\alpha$  makes it the strongest emission line in the optical-NIR window, while for  $z \gtrsim 4$ , Ly $\alpha$  emitters (LAEs; galaxies detected from their emission in Ly $\alpha$ , either by narrow-band photometry or spectroscopy) becomes easier to detect than Lyman-break galaxies (LBGs; galaxies detected from their dropout in wavelengths blueward of the Lyman-break).

From the shape of the Ly $\alpha$  line profile, a variety of valuable information can be obtained about the galaxies emitting it. Ly $\alpha$  resonant scattering theory as well as simulations tell us that, in general, due to the large

optical depth of the neutral hydrogen for a line center photon, the radiation must diffuse to either the blue or the red side of the center, and consequently should escape the interstellar medium (ISM) of its host galaxy in a double-peaked profile. The exact shape of this profile depends on the physical state of the gas, such as its column density, temperature, velocity field, and, in particular, dust contents. Similarly, the strength of the line depends on the stellar population and the dust contents. Notwithstanding the complexity, and indeed sometimes intertwining, of these dependencies, this also makes Ly $\alpha$  a potentially strong source of information.

Whereas absorption processes in gas in many cases are well-known, the effect of dust on the radiative transfer (RT) is still an intensely debated subject. In contrast to gas, laboratory experiments with dust are extremely complex, partly due to the complications involved in replicating the physical environments of the ISM, partly due to our limited knowledge vis-à-vis what actually constitutes cosmic dust.

In the present-day Universe, most dust is formed in the atmospheres of stars on the asymptotic giant branch (AGB) of the Hertzsprung-Russel diagram; the dying phase of stars less massive than  $\sim 8 M_{\odot}$  (e.g. Höfner & Andersen 2007; Mattsson et al. 2008). In these environments the gas is sufficiently cool, yet sufficiently dense that molecules may form and stick together to form dust grains.

However, there is observational evidence that dust is also abundantly present in the early Universe (e.g. Stratta et al. 2007; Coppin et al. 2009). Since the time to reach the AGB phase is of the order of 1 Gyr, something else must have provided the ISM with dust at these

<sup>1</sup> Dark Cosmology Centre, Niels Bohr Institute, University of Copenhagen, Juliane Maries Vej 30, DK-2100, Copenhagen Ø, Denmark; email: pela@dark-cosmology.dk

<sup>3</sup> Excellence Cluster Universe, Technische Universität München, Boltzmannstraße 2, D-85748 Garching, Germany; email: jslarsen@astro.ku.dk

epochs. A promising candidate is supernovae (SNe), the ejecta of which are believed to exhibit favorable conditions for the formation of dust for a short period of time, approximately 600 days after the explosion (e.g. Kottak et al. 2009).

For the Milky Way (MW), as well as the Small and Large Magellanic Clouds (SMC; LMC), the dust extinction curves, i.e. the extinction of light at a given wavelength, are fairly well established (e.g. Bianchi et al. 1996; Nandy et al. 1981; Prevot et al. 1984; Pei 1992), and from the observed color excess  $E(B - V)$  one may then derive the total extinction. The term “extinction” refers to removal of light from the line of sight, be it due to absorption or scattering, and may be characterized by the number  $A_\lambda$  of magnitudes by which the observed object is diminished. For more distant galaxies one is usually obliged to assume similar extinction curves. Since the stellar population of the SMC is younger than that of the LMC, an SMC extinction curve might be expected to describe better the dust in high-redshift galaxies, and has indeed proved to be a good fit in GRB host galaxies (e.g. Jakobsson et al. 2004). Note, however, that the prominent feature at 2175 Å, characteristic of the LMC and MW extinction, has been detected in a few cases also at high redshift (Junkkarinen et al. 2004; Ellison et al. 2006; Srianand et al. 2008; Elíasdóttir et al. 2009).

The overall normalization of extinction curves comes from the observed property that the extinction is found to be very close to proportional with the column density  $N_H$  of hydrogen (e.g. Bohlin et al. 1978). Typically, one combines measurements of  $N_{H_I}$  (and  $N_{H_2}$ ) with the extinction in the V-band,  $A_V$ . In this way, one then knows how much light is extinguished when traveling a given physical distance in space.

However, for light that does not travel directly from the source to the observer, as is the case for resonantly scattered lines like Ly $\alpha$ , the situation becomes more raveled. Not only does the total distance covered by the photons increase by a large and a priori unknown factor, but the photons received from a given point on the sky may also have traveled through physically different environments, in turn implying an unknown and possibly highly increased probability of being absorbed by dust.

For this reason, the observed fact that Ly $\alpha$  radiation nonetheless *does* escape has long puzzled astronomers. The fact that Ly $\alpha$  line profiles are often seen to exhibit a P Cygni-like profile has led to the suggestion that high-velocity outflows of gas are needed to enable escape (Kunth et al. 1998; Östlin et al. 2008; Atek et al. 2008). However, at high redshifts many galaxies are still accreting matter, which should result in an increased *blue* peak. Since this is rarely observed, the shape could be caused by other mechanisms, e.g. IGM absorption.

The angle under which a galaxy is viewed may also affect the amount of observed radiation. Ionizing UV radiation could create “cones” of low neutral hydrogen density emanating from the star-forming regions through which the Ly $\alpha$  can escape (Tenorio-Tagle et al. 1999; Mas-Hesse et al. 2003). Even without these ionized cones, scattering effects alone may cause an anisotropic escape of the Ly $\alpha$  (Laursen & Sommer-Larsen 2007).

Another commonly repeated scenario is a multi-phase medium, where the dust is locked up in cold clouds so

that the photons primarily travel in an ionized, dustless medium (Neufeld 1991; Hansen & Oh 2006). Since continuum radiation travels through the cloud, it would be attenuated more by the dust. This could explain the high Ly $\alpha$  equivalent widths occasionally observed in LAEs (e.g. Malhotra & Rhoads 2002; Rhoads et al. 2003; Shimasaku et al. 2006).

Previous attempts to determine Ly $\alpha$  escape fractions from high-redshift galaxies have mainly been trying to match observed Ly $\alpha$  luminosities with expected, and different methods obtain quite different results. Le Delliou et al. (2005, 2006) found very good agreement between galaxies simulated with the galaxy formation model GALFORM and observational data at  $z = 3-6$ , using a constant escape fraction of  $f_{\text{esc}} = 0.02$  and assuming no IGM absorption. Davé et al. (2006) obtained similar results by matching the Ly $\alpha$  LF of galaxies from their cosmological SPH simulation to the data of Santos et al. (2004), although Nagamine et al. (2008) argued that the data is based on a small sample and that the simulation box size is too small. Matching the simulated Ly $\alpha$  LF to the observed one by Ouchi et al. (2008), Nagamine et al. (2008) themselves obtain  $f_{\text{esc}} \simeq 0.1$ , although the preferred scenario is not that a certain fraction of the Ly $\alpha$  radiation escapes, but rather that a certain fraction of LAEs are “turned on” at a given time (the so-called “duty cycle scenario”). In a similar way, Dayal et al. (2009) find somewhat higher escape fractions at  $z \sim 5.7$  and  $\sim 6.5$  ( $f_{\text{esc}} \sim 0.3$ ), which they use for predicting the LF of LAEs at  $z \sim 7.6$ .

Gronwall et al. (2007) compared inferred Ly $\alpha$  and rest-frame UV continuum SFRs of a large sample of LAEs from the MUSYC (Gawiser et al. 2006) survey and argue that an escape fraction of  $\sim 1/3$  is needed to explain the discrepancy, although Nilsson et al. (2009) pointed out that a missing  $(1+z)$ -factor probably explains the difference. Matching Ly $\alpha$ -inferred SFRs to SED modeling of observed LAEs, Gawiser et al. (2006) found an  $f_{\text{esc}}$  of  $\sim 0.8$ , with a lower limit of 0.2. While SED fitting may not be the most accurate way of estimating SFRs, aiming to match these observations, Kobayashi et al. (2007) obtain similar result theoretically by incorporating the effects of galactic outflows.

In this paper we aim to scrutinize the effect of dust on the Ly $\alpha$  RT by applying the Monte Carlo RT code MOCALATA (Laursen et al. 2009) on a number of simulated galaxies, extracted from fully cosmological TreeSPH simulations. The theoretical aspects of cosmic dust is discussed in §2 and the implementation of this into the RT code in §3. The new version of the code is then tested against physically idealized situations for which analytical solutions exist in §4, before it is applied to realistic simulated galaxies in §5. The results, and the sensitivity of these on the values of different input parameters, are presented in §6 and §7, respectively. Finally, the obtained results are summarized and discussed in §8.

## 2. THEORY OF DUST

Four quantities characterize what impact the dust grains will have on the propagating Ly $\alpha$  photons: the *density*; the (wavelength dependent) *cross-section* of interaction; the *albedo* giving the probability that a photon incident on a dust grain will be scattered rather than absorbed; and finally the *phase function* defining the di-

rection into which a non-absorbed photon is scattered. These quantities will be discussed below.

Dust grains are built up from metals, and thus the dust density is expected to scale with gas metallicity in some fashion. Metals are created in dying stars, i.e. in AGB stars and SNe. For sufficiently dense and cold environments, the neutral metals form molecules which eventually stick together to form dust. No formal definition of the distinction between large molecules and dust grains exist, but may be taken to be of the order of  $\sim 500$  atoms or so.

Depending on the abundances of the individual metals, as well as the physical conditions, a variety of different types of dust may be produced, with regards to both composition and structure, and hence with different scattering properties. Much effort has been put into unraveling the nature of cosmic dust, in particular in explaining the 2175 Å bump. This feature is generally attributed to carbonaceous materials, e.g. graphite, diamonds, and/or polycyclic aromatic hydrocarbons, but still the precise nature remains unknown.

In principle, the result of a photon interacting with a dust grain may be calculated analytically by solving Maxwell's equations, on the basis of the geometry of the particle and its optical properties, i.e. the dielectric functions. This is trivial in the case of simple geometries such as spheres and spheroidals. More general shapes and composites can be modeled by discretizing the grain into a large number of dipoles; the so-called *discrete dipole approximation* (Purcell & Pennypacker 1973; Draine 1988), but for the complex and, more importantly, uncertain or unknown shape of realistic grains, this is not feasible.

Had we full knowledge of the relevant properties of dust, a distribution of the various species could be calculated in simulated galaxies, and the radiative transfer could then be realized by computing the total optical depth of the ISM as a sum of all contributors, and determining for each scattering the kind of particle responsible for the scattering. However, lacking a sound theory of the formation of dust grains, in particular in the high-redshift Universe, we take a different approach: although the exact nature of cosmic dust is not known, the average extinction — and hence the cross-sectional area — of dust as a function of wavelength is known for many different sightlines through the SMC and the LMC (e.g. Gordon et al. 2003). Since the metallicity of the Magellanic Clouds is fairly well known, the extinction curve of the SMC (or LMC) can be scaled to the metallicity of the simulated galaxies, thus yielding the extinction in the simulations.

### 2.1. Cross-section

Observationally, the extinction  $A_V$  in the  $V$ -band is found to have a surprisingly constant proportionality with the column density of hydrogen from sightline to sightline within the MW (e.g. Massa & Fitzpatrick 1986; Fitzpatrick & Massa 2007). Similar results, but with different normalizations, are found for the SMC and the LMC (Gordon et al. 2003). Accordingly, the cross-section  $\sigma_d(\lambda)$  of dust may be conveniently expressed as an effective cross-section *per hydrogen atom*, thus eliminating any assumptions about the size distribution, shape, etc., and merely relying on observed extinction curves. The optical depth  $\tau_d$  of dust when traveling a distance  $r$

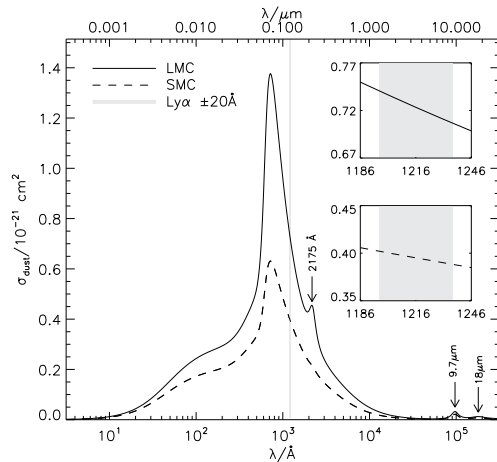


FIG. 1.— Extinction cross-section fits to the observed extinction curves of the LMC (*solid*) and the SMC (*dashed*). The difference in amplitude is mainly due to the SMC being less metal-rich than the LMC. The vertical, grey-shaded area is the region inside which the (rest-frame) Ly $\alpha$  line is expected to fall. The two insets show a zoom-in of this region on the extinction curves (*top*: LMC, *bottom*: SMC), demonstrating the linearity across the Ly $\alpha$  line.

through a region of hydrogen density  $n_H$  is then

$$\tau_d = n_H r \sigma_d = N_H \sigma_d. \quad (1)$$

The quantity usually measured is  $A_\lambda/N_H$ , and the cross-section is then

$$\sigma_d = \frac{\ln 10}{2.5} \frac{A_\lambda}{N_H} \quad (2)$$

We use the fit to the SMC or LMC extinction curves proposed by Pei (1992), which is an extension of the Mattis, Rumpl, & Nordsieck (1977)-model. The fit is a sum of six terms (Drude profiles) representing a background, a far-ultraviolet (FUV), and a far-infrared (FIR) extinction, as well as the 2175 Å, the 9.7  $\mu\text{m}$ , and the 18  $\mu\text{m}$  extinction features. Based on newer data from Weingartner & Draine (2001), Gnedin et al. (2008) adjusted the fit and added a seventh term to account for the narrow, asymmetric FUV peak in the dust extinction.

Figure 1 shows these fits. The insets show that the extinction curves are very close to being linear in the vicinity of the Ly $\alpha$  line. In fact, in this region it is an excellent approximation to write the cross-section as

$$\sigma_d / 10^{-21} \text{ cm}^2 = \begin{cases} 0.395 + 1.82 \times 10^{-5} (T/10^4 \text{ K})^{1/2} x & \text{for the SMC} \\ 0.723 + 4.46 \times 10^{-5} (T/10^4 \text{ K})^{1/2} x & \text{for the LMC.} \end{cases} \quad (3)$$

Here, we have used the parametrization  $x \equiv (\nu - \nu_0)/\Delta\nu_D$  of the frequency  $\nu$  of the photon, where  $\nu_0$  is the line center frequency and  $\Delta\nu_D$  is the Doppler width of the line (times  $\sqrt{2}$ ) resulting from the thermal motion of the atoms with temperature  $T$ . Note that  $T$  only enters Eq. (3) to account for the temperature dependency of  $x$ ;  $\sigma_d$  itself is independent of  $T$ .

### 2.2. Number density

The reason for the variability of extinction with galaxy, and the non-variability with sightline, is to a large de-

agree the different overall metallicities of the galaxies. Although differences exist within the galaxies, the differences are larger from galaxy to galaxy (Pei 1992). In most of the calculations we will use an SMC curve, but as shown in §7 the result is not very different if an LMC curve is used.

Because the cross-section is expressed as a cross-section per hydrogen atom, the relevant quantity is not dust density, but hydrogen density. However, since in general the metallicity at a given location in a simulated galaxy differs from that of the Magellanic Clouds, the amplitude of the extinction will also differ. Assuming that extinction scales with metallicity, a corresponding pseudo number density  $n_d$  of dust at a given location of hydrogen density  $n_H$  and metallicity  $Z_i$  of element  $i$  can then be calculated as

$$n_d \sim n_H \frac{\sum_i Z_i}{\sum_i Z_{i,0}}, \quad (4)$$

where  $Z_{i,0}$  is the average metallicity of element  $i$  in the galaxy the extinction curve of which is applied. Obviously,  $n_d$  is not a true dust number density, but merely a rescaled hydrogen number density.

On average, the SMC metallicities of the different elements are deficit relative to Solar values by 0.6 dex (e.g. Welty et al. 1997), while the LMC is deficit by 0.3 dex (e.g. Welty et al. 1999). Small metal-to-metal deviations from this exist, but scaling  $Z_i$  to the metallicity of the individual metals, using values from Russell & Dopita (1992), does not change the outcome significantly (cf. §7).

The reason that Eq. (4) is not expressed as a strict equality is that we have so far neglected to differentiate between neutral and ionized hydrogen. Dust grains may be destroyed in a number of ways, e.g. through collisions with other grains, sputtering due to collisions with ions, sublimation or evaporation, or even explosions due to ultraviolet radiation (e.g. Greenberg 1976). These scenarios are all expected to become increasingly important for hotter environments. Accordingly, studies of the interstellar abundances of dust have usually assumed that ionized regions contribute negligibly to the dust density, and merely concerned themselves with measuring column densities of neutral hydrogen, i.e.  $\text{HI} + \text{H}_2$ . Moreover, many metallicity measurements are derived from low-resolution spectra not capable of resolving and characterizing various components of the ISM. As discussed in §2.2.1, dust is also observed in regions that are primarily ionized, and since the bulk of the  $\text{Ly}\alpha$  photons is produced in the proximity of hot stars with a large intensity of ionizing UV radiation, even a little dust associated with the ionized gas might affect the results.

Hence, we assume that the amount of dust scales with the total amount of neutral hydrogen *plus* some fraction  $f_{\text{ion}}$  of the ionized hydrogen, and Eq. (4) should then be

$$n_d = (n_{\text{HI}} + f_{\text{ion}} n_{\text{HII}}) \frac{\sum_i Z_i}{\sum_i Z_{i,0}} \quad (5)$$

Of course, this is not a physical number density of dust grains but with this expression, the total optical depth of gas and dust as seen by a propagating photon traveling a distance  $r$  is

$$\tau_{\text{tot}} = r(n_{\text{HI}}\sigma_x + n_d\sigma_d), \quad (6)$$

where the neutral hydrogen cross-section  $\sigma_x$  is given by

$$\sigma_x = f_{12} \frac{\pi e^2}{m_e c \Delta\nu_D} \phi(x). \quad (7)$$

Here  $f_{12}$  is the  $\text{Ly}\alpha$  oscillator strength,  $e$  and  $m_e$  is the charge and the mass of the electron, and  $c$  is the speed of light. The wavelength dependence of the cross-section enters through the line profile  $\phi(x) = H(a, x)/\sqrt{\pi}$ , where  $H(a, x)$  is the Voigt function — the convolution of a thermal and a natural broadening of the line — with  $a = \Delta\nu_L/2\Delta\nu_D$  being the ratio between the natural and (twice) the thermal line width (the “damping parameter”).

In principle, the summation term in Eq. (5) should also include a term accounting for the fact that the dust-to-metal ratio  $f_{\text{dm}}$  in a given cell may be different from that for which the empirical data exist. In the Milky Way and the Magellanic Clouds,  $f_{\text{dm}} \simeq 1$  for most metals, i.e. roughly 1/2 of the metals is condensed to dust grains. The depletion patterns in high-redshift galaxies are not well constrained, but no measurements suggest that it should be substantially different from the local Universe. In fact Pei, Fall, & Hauser (1998) interpret the depletion patterns of Cr and Zn measured in damped  $\text{Ly}\alpha$  systems by Pettini et al. (1997) as giving  $f_{\text{dm}} \simeq 1$  for  $z \lesssim 3$ . Similarly, fitting depletion patterns of eight elements in GRB host galaxies, Savaglio et al. (2003) find  $f_{\text{dm}} \simeq 1$ .

### 2.2.1. Dust in ionized gas

Ionized gas is found in a number of physically distinct locations throughout the Universe. Compact HII regions, or Strömgren spheres, surround young, hot stars, while more diffuse HII is a part of the ISM. Larger HII “bubbles” are formed around regions of massive star formation due not only to ionizing radiation from the stars but also to the energy deposited in the ISM from supernova feedback. Outside the galaxies, the IGM is predominantly ionized at  $z \lesssim 5-6$ . Observations show or indicate the presence of dust in all of these media. While generally lower than in the neutral gas, inferred dust-to-gas mass ratios ( $f_{\text{dg}}$ ) in ionized gas span a range from roughly equal to the typically assumed MW ISM value of  $\sim 0.01$ , to upper limits of  $\sim 10^{-4}$  times lower than this.

Based on 45–180  $\mu\text{m}$  (FIR) spectroscopy, Aannestad & Emery (2001) found the Galactic HII region S125 to be strongly depleted of dust, with a dust-to-gas ratio of  $f_{\text{dg}} \leq 10^{-6}$ , while Smith et al. (1999), using MIR imaging and spectroscopy, inferred a dust-to-gas ratio of the Galactic HII region RCW 38 of  $10^{-5}$  to  $10^{-4}$ . On the other hand, using FIR spectroscopy Chini et al. (1986) found 12 HII regions to be dust-depleted by “only” a factor of 10 relative to the MW ISM (i.e.  $f_{\text{dg}} \sim 10^{-3}$ ), while from FIR photometry, Harper & Low (1971) found the median dust-to-ionized-gas ratio of seven HII regions to be close to 0.01.

For the more diffuse HII gas that comprises part of the ISM, most obtained extinction curves in a sense already include the contribution of HII to  $n_d$ , although its quantity is not revealed when measuring HI column densities. Hence, any value of  $f_{\text{ion}}$  for the diffuse ISM larger than 0 would account twice for the ionized gas.

The dominant destruction mechanism of dust is prob-

ably shock waves, associated with, e.g., high-velocity clouds and SN winds (Draine & Salpeter 1979a,b). However, since SNe are thought to be the prime creator of dust at high redshifts, the HII bubbles in the vicinity of massive star-forming regions cannot be entirely void of dust, and observational evidence of dust related to SN remnants (SNR) and starburst regions does indeed exist. Using MIR imaging, Bouchet et al. (2006) determined the dust-to-gas ratio of SN 1987A to be  $\sim 5 \times 10^{-3}$ . Somewhat lower results are found in Kes 75 ( $\sim 10^{-3}$  from FIR and X-ray, Morton et al. 2007) and in Kepler’s SN ( $\sim 10^{-3}$  from IR and bremsstrahlung, Contini 2004). On larger scales, the hostile environments imposed by the SNe and ionizing radiation will reduce the dust density in starburst regions. Fitting continuum SEDs, Contini & Contini (2004) found that  $10^{-4} \lesssim f_{\text{dg}} \lesssim 10^{-2}$  in various starburst regions in a sample of seven luminous infrared galaxies. However, such regions are not ionized to the same level as compact HII regions and SNRs, and as argued in the case of the diffuse HII, the scaling of dust with HI to some extent already accounts for the HII.

Various feedback processes are also responsible for expelling a non-vanishing amount of metals and dust into the IGM, although inferred dust-to-gas ratios tend to be small: from IR-to-X-ray luminosities, Giard et al. (2008) inferred a dust-to-gas ratio of a few to 5 times  $10^{-4}$ , as did Chelouche et al. (2007) by comparing photometric and spectroscopic properties of quasars behind SDSS clusters. Higher (dust-to-HI  $\sim 0.05$  in the M81 Group, Xilouris et al. 2006) — possibly expelled from the starburst galaxy M82 — and lower ( $f_{\text{dg}} \sim 10^{-6}$  in the Coma cluster and even less in five other Abell clusters, Stickel et al. 2002) values are also found. Additionally, sputtering by the hot halo gas may tend to destroy primarily small grains, leading to a flattening of the extinction curve in the UV; at the Ly $\alpha$  wavelength, this may reduce the average cross-section by a factor of 4–5 (Aguirre et al. 2001).

In summary, the factor  $f_{\text{ion}}$  is a practical way of modeling the destruction of dust in physically “hostile” environments. For simplicity, in the RT code we will not distinguish between HII in various regions but merely settle on an average dust-to-gas ratio of ionized gas of  $\sim 10^{-4}$ ; that is we set  $f_{\text{ion}} = 0.01$ . In §7, we investigate the effect of other values of  $f_{\text{ion}}$  and find that using 0.01, the resulting escape fractions lie approximately midway between those found when using  $f_{\text{ion}} = 0$  (corresponding to the *complete* destruction of dust in regions where hydrogen is ionized) and  $f_{\text{ion}} = 1$  (corresponding to no destruction of dust at all). Moreover, these extreme values does not seem to change  $f_{\text{esc}}$  by more than  $\sim 25\%$ .

### 2.3. Albedo

When a photon interacts with a dust grain, it may be either absorbed or scattered. The efficiency with which the dust grain scatters radiation is dependent on the composition (material, shape, etc.) of the dust and on the wavelength of the incident photon. If the photon is not scattered (i.e. emitted with the same wavelength as the incident photon), it is absorbed. In this case it is converted into heat and re-emitted at a later time as infrared radiation. Expressing the total cross-section as a sum of a scattering cross-section  $\sigma_s$  and an absorbing

cross-section  $\sigma_a$ , such that  $\sigma_d = \sigma_s + \sigma_a$ , the albedo  $A$  of the dust is defined as

$$A = \frac{\sigma_s}{\sigma_d}. \quad (8)$$

The albedo of dust has been investigated observationally from reflection nebulae (e.g. Calzetti et al. 1995) and diffuse galactic light (e.g. Lillie et al. 1976). At the Ly $\alpha$  wavelength,  $A$  lies approximately between 0.3 and 0.4 for various size distributions fitted to the LMC and SMC, assuming that the dust is made mainly of graphite and silicates (Pei 1992; Weingartner & Draine 2001). We adopt an albedo of  $A = 0.32$  (from Li & Draine 2001), but investigate the impact of using other values in §7.

### 2.4. Phase function

If a photon is not absorbed, it is scattered. The probability distribution of deflection angles  $\theta$  from its original path is given by the phase function. For reasons of symmetry, the scattering must be symmetric in the azimuthal angle  $\phi$  (unless the grains are collectively oriented in some preferred direction due to, e.g., magnetic field lines), but in general this is not the case in  $\theta$ . In fact, dust is often observed to be considerably forward scattering [e.g. in reflection nebulae (Burgh et al. 2002), diffuse galactic light (Schiminovich et al. 2001), and interstellar clouds (Witt & Oliveri 1990)]. This asymmetric scattering may be described by the Henyey-Greenstein (1941) phase function

$$P_{\text{HG}}(\mu) = \frac{1}{2} \frac{1 - g^2}{(1 + g^2 - 2g\mu)^{3/2}}, \quad (9)$$

where  $\mu = \cos\theta$  and  $g = \langle \mu \rangle$  is the asymmetry parameter. For  $g = 0$ , Eq. (9) reduces to isotropic scattering, while  $g = 1$  ( $-1$ ) implies complete forward (backward) scattering.  $g$  is a function of wavelength, but for  $\lambda$  close to that of Ly $\alpha$ , Li & Draine (2001) found that  $g = 0.73$ . Again, other values are investigated in §7.

## 3. IMPLEMENTATION IN MONTE CARLO CODE

The numerical code, MOCALATA, used to conduct the radiative transfer of Ly $\alpha$ , is described in detail in Laursen et al. (2009). To understand how the effect of dust is implemented, a brief summary of the concepts of the code is given below.

The non-dusty version of the code assumes an arbitrary distribution of neutral hydrogen density  $n_{\text{HI}}$ , Ly $\alpha$  emissivity  $L$ , gas temperature  $T$  and velocity field  $\mathbf{v}_{\text{bulk}}$ . The physical parameters, typically resulting from a cosmological simulation, are assigned in a cell-based structure, where any cell may be refined, i.e. split up in eight sub-cells, recursively to an arbitrary level of refinement, thus allowing for investigation of a detailed structure.

The basic principles of the code are as follows: photons are emitted from a random point in space, weighted according to the emissivity at that particular point, i.e. a given photon has a probability  $L_i/L_{\text{tot}}$  of being emitted from the  $i$ ’th cell, where  $L_{\text{tot}}$  is the total Ly $\alpha$  luminosity of the system. It is emitted in a random direction, with a frequency close to the Ly $\alpha$  line center.

The photon travels through the gas, traversing an optical depth  $\tau$  with a probability  $e^{-\tau}$ , before it is scattered

on a hydrogen atom. Re-emitted in a new, random direction, weighted according to an appropriate phase function, it continues its journey until it escapes the computational box. At each scattering, the velocity (thermal + bulk) of the atom will Doppler shift the frequency of the photon, so that it diffuses not only in real but also in frequency space. This procedure is then repeated for a number  $n_{\text{ph}}$  of photons sufficient to provide good statistic for the quantities of interest (several 1000s, or millions, depending on the desired output).

For each photon and for each scattering, the probability that the photon escape in the directions of six virtual observers located at a distance of the luminosity distance of the galaxy along the three Cartesian axes is computed and added to an associated array (a “CCD”) of three dimensions; two spatial and one frequential, so that a full spectrum is obtained for each pixel in the image.

### 3.1. Metallicity normalization

In addition to the parameters  $n_{\text{HI}}$ ,  $L$ ,  $T$  and  $\mathbf{v}_{\text{bulk}}$ , every cell has an ionized hydrogen density  $n_{\text{HII}}$  and a metallicity  $Z_i$  of the different elements associated with it, from which a dust density (per hydrogen atom)  $n_{\text{d}}$  is calculated according to Eq. (5).

With a randomly drawn optical depth to be covered by a photon, the distance  $r$  traveled can then be calculated as

$$r = \frac{\tau}{n_{\text{HI}}\sigma_x + n_{\text{d}}\sigma_{\text{d}}}. \quad (10)$$

Having reached this distance, a random number  $\mathcal{R} \in [0, 1]$  (a “univariate”) determines whether the photon hits a hydrogen atom or a dust grain by comparing it to the ratio  $\varrho = n_{\text{d}}\sigma_{\text{d}}/(n_{\text{HI}}\sigma_x + n_{\text{d}}\sigma_{\text{d}}) = \tau_{\text{d}}/(\tau_x + \tau_{\text{d}})$ ; if  $\mathcal{R} \leq \varrho$ , the interaction is caused by dust. In this case a second univariate is compared to the albedo of the dust grain, dictating whether the photon is absorbed, thus terminating the journey of this particular photon, or scattered, in which case it is re-emitted in a random direction given by Eq. (9).

Various acceleration schemes were implemented in the non-dusty Ly $\alpha$  RT; the extension of these to the dusty version is discussed in App. A.

### 4. TESTING THE CODE

Neufeld (1990) provided an analytical expression for the escape fraction of photons emitted from inside a “slab” (i.e. finite in the  $z$ -direction and infinite in the  $xy$ -direction) of an absorbing medium. The solution, which is valid for very high optical depths ( $a\tau_0 \gtrsim 10^3$ , where  $\tau_0$  is the optical depth of neutral hydrogen from the center to the surface of the slab) and in the limit  $(a\tau_0)^{1/3} \gg \tau_{\text{a}}$ , where  $\tau_{\text{a}}$  is the absorption optical depth of dust, is

$$f_{\text{esc}} = \frac{1}{\cosh \left[ \zeta' \sqrt{(a\tau_0)^{1/3} \tau_{\text{a}}} \right]}, \quad (11)$$

where  $\zeta' \equiv \sqrt{3}/\zeta\pi^{5/12}$ , with  $\zeta \simeq 0.525$  a fitting parameter. Figure 2 shows the result of a series of such simulations, compared to the analytical solution.

Various AMR grid configurations were tested. Of course, the physical parameters such as  $n_{\text{HI}}$ ,  $n_{\text{d}}$ , and  $T$  of a cell does not depend on the refinement level, but the acceleration schemes discussed in App. A do.

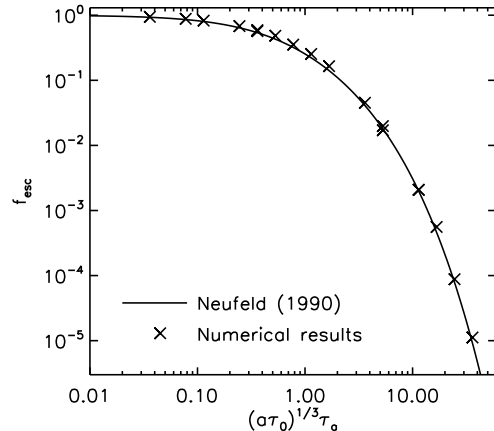


FIG. 2.— Escape fractions  $f_{\text{esc}}$  of photons emitted from the center of a semi-infinite slab of gas damping parameter  $a$ , hydrogen optical depth  $\tau_0$ , and dust absorbing optical depth  $\tau_{\text{a}}$ , compared to the analytical solution in Eq. (11).

### 5. SIMULATIONS

To investigate the fraction of emitted Ly $\alpha$  photons that escapes galaxies at high redshift, the code was applied to a number of different simulated high-resolution galaxies, emerging from a fully cosmological N-body/hydrodynamical TreeSPH simulation. This code was described in detail in Sommer-Larsen et al. (2003) and Sommer-Larsen (2006), and summarized in Laursen et al. (2009). Here, we will only briefly review the basic characteristics of the code:

The numerical simulations are first carried out at low resolution, but in a large volume of space. Subsequently, interesting galaxy-forming regions are re-simulated at high resolution. In addition to hydrogen and helium, the code follows the chemical evolution of C, N, O, Mg, Si, S, Ca, and Fe.

The Ly $\alpha$  emission is produced by three different processes (see also Laursen & Sommer-Larsen 2007), viz. from recombinations in photoionized regions around massive stars (responsible for  $\sim 90\%$  of the total Ly $\alpha$  luminosity), gravitational cooling of infalling gas ( $\sim 10\%$ ), and a metagalactic UV background (UVB) photoionizing the external parts of the galaxy ( $\sim 1\%$ ).

The UVB field is assumed to be that given by Haardt & Madau (1996), where the gas is treated as optically thin to the UV radiation until the mean free path of a UV photon at the Lyman limit becomes less than 0.1 kpc, at which point the gas is treated as optically thick and the UV field is “switched off”.

A far more realistic UV RT scheme was implemented in the code by Razoumov & Sommer-Larsen (2006, 2007) which alters the ionization state and temperature field of the gas somewhat. However, as was concluded in Laursen et al. (2009), the effect of the improved UV RT only results in minor changes for the non-dusty Ly $\alpha$  RT. Moreover, as shown in §7 it does not alter  $f_{\text{esc}}$  drastically, and has thus not been applied in the present paper.

Nine individual galaxies are extracted from the cosmological simulation at redshift  $z = 3.6$  — at which time the Universe was 1.8 Gyr old — to be used for the Ly $\alpha$  RT. These galaxies are representative of typical galaxies in the sense that they span three orders of magnitudes in

mass, the most massive eventually evolving into a disk galaxy with circular speed  $V_c \simeq 300 \text{ km s}^{-1}$  at  $z = 0$ . The numerical and physical properties of these galaxies are listed in Tab. 1 and Tab. 2, respectively.

Since the Ly $\alpha$  RT code is cell-based, the relevant physical properties of the particles are interpolated from the 50 nearest neighboring particles onto a grid of base resolution  $128^3$  cells. Dense cells are subdivided in eight cells, which are further refined until no cell contains more than ten particles. Achieving the same resolution without this adaptively refined mesh would require from  $\sim 16\,000^3$  to  $\sim 65\,000^3$  cells; infeasible with present-day’s computer facilities.

This level of resolution is rather crucial to the escape of the Ly $\alpha$  photons. As is evident from Fig. 3, the bulk of the photons is produced in regions of very high column densities, exceeding  $N_{\text{HI}} = 10^{23} \text{ cm}^{-2}$ . Even for metallicities of only  $1/100 Z_{\odot}$ , Eq. (11) implies an escape fraction of  $\sim 10^{-5}$  (for  $T \sim 10^4 \text{ K}$ ). However, Eq. (11) assumes a *homogeneous* medium. As was argued by Neufeld (1991) and investigated numerically by Hansen & Oh (2006), in a multi-phase medium, the Ly $\alpha$  photons may escape more easily. In the (academic) case of all the dust residing in cool, dense clouds of neutral hydrogen which, in turn, are dispersed in a hot, empty medium, the Ly $\alpha$  escape fraction may approach unity. The reason is that the photons will scatter off of the surface before penetrating substantially into the clouds, thus effectively confining their journey to the dustless intercloud medium.

Although this scenario is obviously very idealized, the presence of an inhomogeneous medium undoubtedly reduces the effective optical depth, and has indeed been invoked to explain unusually large Ly $\alpha$  equivalent widths (e.g. Finkelstein et al. 2008). Nevertheless, it is not clear to which degree the escape fraction of Ly $\alpha$  will actually be affected. Other scenarios have been proposed to explain the apparent paradoxical escape of Ly $\alpha$ , e.g. galactic superwinds, as discussed in the introduction. Here we present the first calculations of  $f_{\text{esc}}$ , based on fully cosmological, numerical galaxy formation models, demonstrating that generally of the order 5%–30% of the Ly $\alpha$  radiation escapes the galaxies at redshifts  $z \sim 3$ –4, even if no particularly strong winds are present.

## 6. RESULTS

In the discussion of the results, we will first focus on one particular galaxy, observed from one direction. We arbitrarily chose K15, which at  $z = 0$  becomes an M31-sized disk galaxy, and we chose the observer placed toward negative values on the  $z$ -axis (the  $z_-$ -direction), the direction in which most radiation escapes. In §6.4 we proceed to discuss the extent to which the results are representative for other galaxies and directions.

### 6.1. Where are the photons absorbed?

Figure 4 shows the surface brightness (SB) maps of the galaxy K15. The left panel shows how the galaxy would look if the gas were dust-free, while the right panel displays the more realistic case of a dusty medium. Comparing the two images, it is seen that the regions that are affected the most by dust are the most luminous regions. This is even more evident in Fig. 5, where the

azimuthally averaged profiles of the SB maps are shown.

The reason for this is two-fold: the most luminous regions are the regions where the stars reside. Because dust is produced by stars, this is also where most of the dust is. Since the stars, in turn, are born in regions of high hydrogen density, the RT is here associated with numerous scatterings, severely increasing the path length of the photons, and consequently increasing further the probability of being absorbed.

The SB in the less luminous regions also decreases. Although dust also resides here, having been expelled by the feedback of starbursts, only little absorption actually takes place here. The decrease in luminosity is mainly due to the photons being absorbed in the high density regions that would otherwise have escaped the inner regions and subsequently been scattered by the circumambient neutral gas into the direction of the observer. This is also discernible from Fig. 6 that displays an image of the absorbed photons.

Figure 7 shows the *source* Ly $\alpha$  emissivity of the photons that are eventually absorbed, compared to that of the photons that eventually escape. Here it becomes evident that virtually all the absorbed photons are emitted from the central parts, while photons that escape are emitted from everywhere. In particular, the radiation produced through gravitational cooling escapes more or less freely.

### 6.2. Effect on the emergent spectrum

Due to the high opacity of the gas for a Ly $\alpha$  photon at line center, photons generally diffuse in frequency to either the red or the blue side in order to facilitate escape. Consequently, the spectrum of the radiation escaping a dustless medium is characterized by a double-peaked profile. The broadening of the wings is dictated by the product  $a\tau_0$  (Harrington 1973), i.e. low temperatures and, in particular, high densities force the photons to diffuse far from line center. Since such conditions are typical of the regions where the bulk of the photons is absorbed, the emergent spectrum of a dusty medium is severely narrowed, although the double-peaked feature persists. Figure 8 displays the spatially integrated spectra of the dustless and the dusty version of K15.

This interesting result shows that even though the dust is effectively grey (the small wavelength dependence of Eq. (3) does not produce substantially different results from using a completely wavelength *independent* cross-section), the emergent spectrum is affected in a highly “non-grey” fashion: whereas the escape fraction of the inner part of the spectrum is of the order 50%, it rapidly drops when moving away from the line center.

### 6.3. Escape fraction

In the  $z_-$ -direction of K15, the fraction of Ly $\alpha$  photons escaping is 0.14. As mentioned earlier, the  $z_-$ -direction is the direction into which most radiation escapes — without dust, this direction is  $\sim 3$  times as luminous as the  $x_-$ -direction, which is where the least radiation is emitted. Including dust, because the brightest regions are affected the most, the ratio between the luminosity in the least and the most luminous directions is somewhat reduced, although  $z_-$  is still more than twice as bright as  $x_-$ .

TABLE 1  
CHARACTERISTIC QUANTITIES OF THE SIMULATIONS

Galaxy	S33sc	K15	S29	K33	S115	S87	S108	S115sc	S108sc
$N_{p,tot}$	$1.2 \times 10^6$	$2.2 \times 10^6$	$1.1 \times 10^6$	$1.2 \times 10^6$	$1.3 \times 10^6$	$1.4 \times 10^6$	$1.3 \times 10^6$	$1.3 \times 10^6$	$1.3 \times 10^6$
$N_{SPH}$	$5.5 \times 10^5$	$1.0 \times 10^6$	$5.1 \times 10^5$	$5.5 \times 10^5$	$6.4 \times 10^5$	$7.0 \times 10^5$	$6.3 \times 10^5$	$6.4 \times 10^5$	$6.3 \times 10^5$
$m_{SPH}, m_{star}$	$5.4 \times 10^5$	$9.3 \times 10^4$	$9.3 \times 10^4$	$9.3 \times 10^4$	$1.1 \times 10^4$	$1.2 \times 10^4$	$1.2 \times 10^4$	$2.6 \times 10^3$	$1.5 \times 10^3$
$m_{DM}$	$3.0 \times 10^6$	$5.2 \times 10^5$	$5.2 \times 10^5$	$5.2 \times 10^5$	$6.6 \times 10^4$	$6.5 \times 10^4$	$6.5 \times 10^4$	$1.4 \times 10^4$	$8.1 \times 10^3$
$\epsilon_{SPH}, \epsilon_{star}$	344	191	191	191	96	96	96	58	48
$\epsilon_{DM}$	612	340	340	340	170	170	170	102	85
$l_{min}$	18	10	10	10	5	5	5	3	2.5

NOTE. — Total number of particles ( $N_{p,tot}$ ), number of SPH particles only ( $N_{SPH}$ ), masses ( $m$ ), gravity softening lengths ( $\epsilon$ ), and minimum smoothing lengths ( $l_{min}$ ) of dark matter (DM), gas (SPH), and star particles used in the simulations. Masses are measured in  $h^{-1}M_{\odot}$ , distances in  $h^{-1}$ pc.

TABLE 2  
PHYSICAL PROPERTIES OF THE SIMULATED GALAXIES

Galaxy	S33sc	K15	S29	K33	S115	S87	S108	S115sc	S108sc
$SFR/M_{\odot} \text{ yr}^{-1}$	70	16	13	13	0.5	0.46	1.62	$3.7 \times 10^{-3}$	$1.7 \times 10^{-3}$
$M_{*}/M_{\odot}$	$3.4 \times 10^{10}$	$1.3 \times 10^{10}$	$6.0 \times 10^9$	$6.5 \times 10^9$	$2.5 \times 10^8$	$1.8 \times 10^8$	$4.9 \times 10^8$	$2.0 \times 10^7$	$5.9 \times 10^6$
$M_{vir}/M_{\odot}$	$7.6 \times 10^{11}$	$2.8 \times 10^{11}$	$1.7 \times 10^{11}$	$1.3 \times 10^{11}$	$2.5 \times 10^{10}$	$2.1 \times 10^{10}$	$2.6 \times 10^9$	$4.9 \times 10^9$	$3.3 \times 10^8$
$r_{vir}/\text{kpc}$	63	45	39	35	20	19	10	12	5
[O/H]	-0.08	-0.30	-0.28	-0.40	-1.22	-1.28	-0.51	-1.54	-1.64
$V_c(z=0)/\text{km s}^{-1}$	300	245	205	180	125	132	131	50	35
$L_{Ly\alpha}/\text{erg s}^{-1}$	$1.6 \times 10^{44}$	$4.5 \times 10^{43}$	$2.9 \times 10^{43}$	$2.5 \times 10^{43}$	$1.3 \times 10^{42}$	$1.1 \times 10^{42}$	$2.6 \times 10^{42}$	$4.9 \times 10^{40}$	$3.2 \times 10^{39}$
$L_{\nu,UV}/\text{erg s}^{-1} \text{ Hz}^{-1}$	$5.0 \times 10^{29}$	$6.7 \times 10^{28}$	$9.3 \times 10^{28}$	$5.5 \times 10^{28}$	$3.6 \times 10^{27}$	$3.3 \times 10^{27}$	$1.2 \times 10^{28}$	$2.6 \times 10^{25}$	$1.2 \times 10^{25}$

NOTE. — Star formation rates (SFRs), stellar masses ( $M_{*}$ ), virial masses ( $M_{vir}$ ), virial radii ( $r_{vir}$ ), metallicities ([O/H]), circular velocities ( $V_c$ ), Ly $\alpha$  luminosities ( $L_{Ly\alpha}$ ), and UV luminosities ( $L_{\nu,UV}$ ) for the simulated galaxies. All quoted values correspond to a redshift of  $z = 3.6$ , except  $V_c$  which is given for  $z = 0$ .

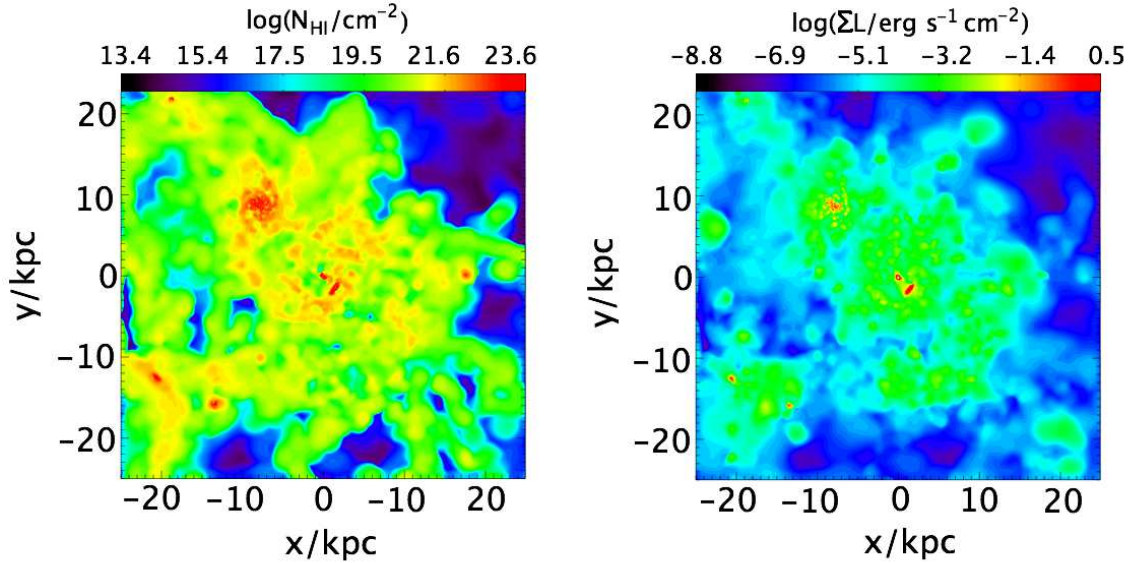


FIG. 3.— Neutral hydrogen column density ( $N_{HI}$ ) map (*left*) and integrated source Ly $\alpha$  emissivity ( $\Sigma L$ ) map (*right*) of the simulated galaxy K15. The vast majority of the photons are seen to be emitted in the very dense environments. According to the analytical solution for the Ly $\alpha$  escape fraction provided by Neufeld (1990, Eq. (11) in this paper), virtually all photons should be absorbed by dust, but taking into account the clumpiness of the ISM allows for much higher escape fractions.



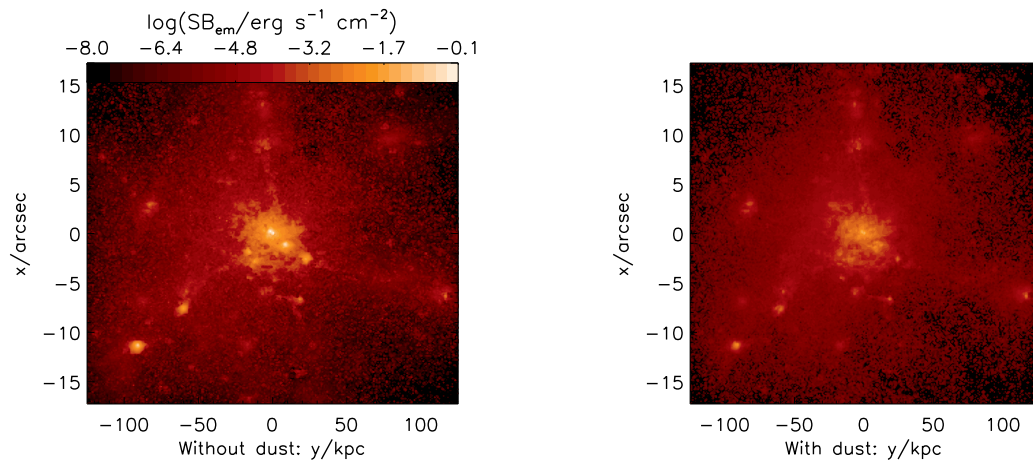


FIG. 4.— Surface brightness maps of the galaxy K15, as viewed from the negative  $z$ -direction, without dust (*left*) and with dust (*right*). Including dust in the radiative transfer affects primarily the most luminous regions.

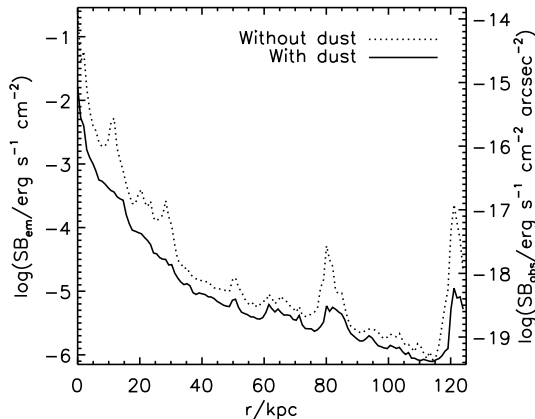


FIG. 5.— Surface brightness (SB) profile of the galaxy K15, again with dust (*solid*) and without dust (*dotted*). Left ordinate axis gives the SB as measured at the source while right ordinate gives the values measured by an observer at a distance given by the luminosity distance of the galaxy. The decrease in SB in the less luminous regions is noticeable. However, this decrease is for the most part *not* due to photons being absorbed in the hot and tenuous circumgalactic medium but rather reflects a lack of photons that in the case of no dust would have escaped the luminous regions and subsequently scattered on neutral hydrogen in the direction of the observer.

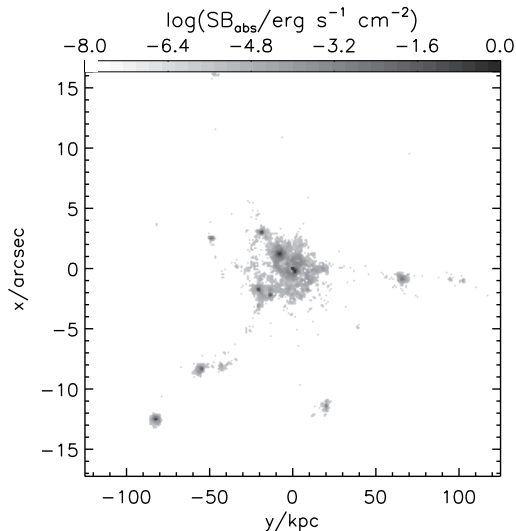


FIG. 6.— Image of the locations of absorption of the  $\text{Ly}\alpha$  radiation that does *not* escape K15. Effectively, this image shows the column density of dust.

The sky-averaged escape fraction for K15 is 0.16. Recall that in these simulations SMC dust has been applied. However, as discussed in §7 using LMC dust does not alter the results significantly.

#### 6.4. General results

The results found in the previous sections turn out to be quite illustrative of the general outcome of  $\text{Ly}\alpha$  RT in a dusty medium: photons are absorbed primarily in the dense, luminous regions, leading to a reduced luminosity in these parts of the galaxies and effectively smoothing out prominent features. Furthermore, the wings of the spectrum experience a strong cut-off.

##### 6.4.1. Anisotropic escape of $\text{Ly}\alpha$

In general, the radiation does *not* escape isotropically; the ratio of luminosities observed from different directions ranges from  $\sim 1.5$  to  $\sim 4$ . Without dust, these ratios are somewhat higher, up to a factor of  $\sim 6$ . Although “bright directions” are affected more by the dust than less bright directions, the variation in  $f_{\text{esc}}$  as a function of direction is not large, and not very different from the sky-averaged  $f_{\text{esc}}$ .

##### 6.4.2. Correlation of $f_{\text{esc}}$ with galactic mass

Figure 9 shows the escape fractions of the galaxies as a function of the virial masses of the galaxies. Despite a large scatter, and although the sample is too small to say anything definite, the figure indicates that  $f_{\text{esc}}$  decreases with increasing mass of the host galaxy. In addition to the nine high-resolution galaxies [of which two appear in two “versions”; with a Salpeter (1955) and with a Kroupa (1998) initial mass function (IMF)], 17 galaxies from a low-resolution (Kroupa) simulation are shown. These galaxies were chosen according to the criterion that the number of star particles is  $\geq 1000$  to ensure an acceptable resolution. Similar results are found for the escape of ionizing UV radiation (Razoumov & Sommer-Larsen 2009). The reason is probably a combination of two mechanisms: small galaxies have a lower metallicity and hence less dust than large galaxies. Furthermore, due to their smaller gravitational potential the stellar feedback will “puff up” small galaxies relatively more and make them less ordered, thus reducing the column density of both dust and gas.

##### 6.4.3. Narrowing of the spectrum

Figure 10 shows the emergent spectra of the studied galaxies, arranged according to virial mass. In general, the same trend as for K15 is seen for all galaxies: the dust primarily affects the wings of the profiles. As discussed in §6.2, the reason is that the wings of the  $\text{Ly}\alpha$  profile are comprised by photons originating in the very dense regions of the galaxy having to diffuse far from the line center in order to escape, and since this is also where the most of the dust is residing, these photons have a larger probability of being absorbed. For the two least massive galaxies, S108sc and S115sc, the ISM is neither very dense nor very metal-rich, meaning that photons escape rather easily. Consequently, the line is not particularly broadened and most of the photons escape the galaxies.

##### 6.4.4. Extended surface brightness profile

The fact that more photons are absorbed in the bright regions tend to “smooth out” the SB profiles of the galaxies. Young galaxies have often been found to be more extended on the sky when observed in  $\text{Ly}\alpha$ , compared to continuum band observation (Møller & Warren 1998; Fynbo et al. 2001, 2003; Nilsson et al. 2007). Laursen & Sommer-Larsen (2007) found that, even without dust, resonant scattering itself may cause an extended  $\text{Ly}\alpha$  SB profile. Including dust merely adds to this phenomenon, since steep parts of the profile are flattened. Figure 11 shows this effect for three arbitrarily chosen galaxies and directions. Extended emission is seen also on larger scales (tens of kpc),

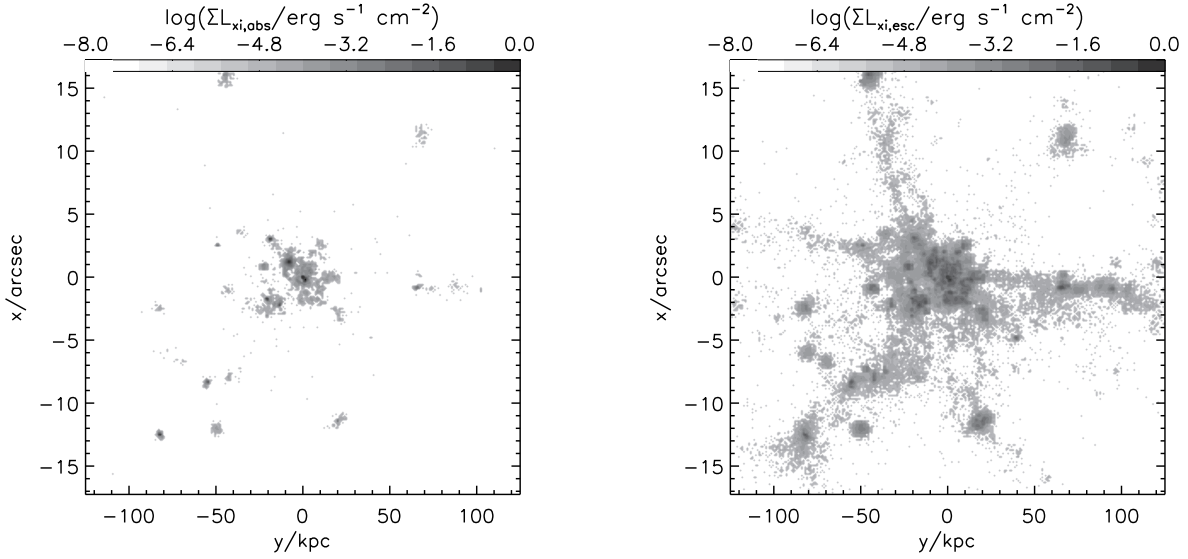


FIG. 7.— Surface brightness maps of the source Ly $\alpha$  emissivity, of the photons that are eventually absorbed (*left*), and the photons that eventually escape (*right*). These images clearly show that absorbed and escaping photons do not in general probe the same physical domains.

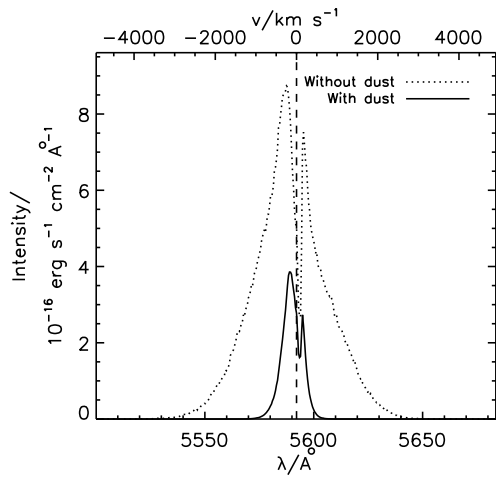


FIG. 8.— Observed spectral distribution of the radiation escaping the galaxy K15 in the negative  $z$ -direction, with (*solid*) and without (*dotted*) dust. The vertical, dashed line marks the Ly $\alpha$  line center. Although the dust is close to being grey, the spectrum is not affected in the same way at all wavelengths; the inner parts are only diminished by a factor of  $\sim 2$ , while the wings are severely reduced. The reason is that the photons in the wings are the ones produced in the dense and dusty regions of the galaxy, so these photons have a higher probability of being absorbed.

although this is more likely to be caused by cold accretion onto dark matter halos (Nilsson et al. 2006).

### 6.5. Temporal fluctuations

Many factors play a role in determining the exact value of  $f_{\text{esc}}$ . Although the metallicity, and hence the state of maturity of the galaxy, as well as the size of the galaxy seem to be the most significant property regulating  $f_{\text{esc}}$ , less systematic factors like the specific configuration of gas and stars are also likely to have a large influence. The scatter in Fig. 9 is probably due to this effect. To get an idea of the fluctuations of  $f_{\text{esc}}$  with time, RT calculations were run for snapshots of K15 from 100 Myr before ( $z = 3.8$ ) to 100 Myr after ( $z = 3.5$ ) the one already explored at  $z = 3.6$ . In this relatively short time, neither  $Z$  nor

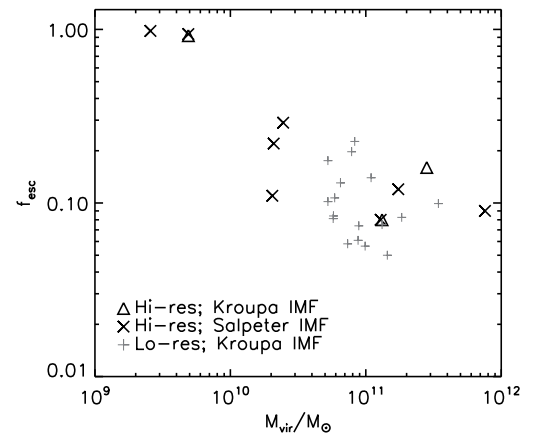


FIG. 9.— Escape fraction  $f_{\text{esc}}$  as a function of galactic virial mass  $M_{\text{vir}}$ . Although the plot exhibits a large scatter, there is a clear trend of  $f_{\text{esc}}$  decreasing with increasing  $M_{\text{vir}}$ .

$M_{\text{vir}}$  should not evolve much, and thus any change should be due to stochastic scatter.

Figure 12 shows the variation of  $f_{\text{esc}}$  during this time interval, demonstrating that the temporal dispersion is of the order 10% on a 10 Myr scale. This suggests that the scatter seen in  $f_{\text{esc}}(M_{\text{vir}})$  (Fig. 9) reflects galaxy-to-galaxy variations rather than  $f_{\text{esc}}$  of the individual galaxies fluctuating strongly with time.

## 7. PARAMETER STUDY

The adopted model of dust clearly involves a multitude of assumptions, some more reasonable than others. To inspect the dependency of the outcome on the values of the parameters a series of simulations of K15 was run, varying the below discussed values. The resulting escape fractions compared to that of the “benchmark” model, used for the simulations in Sec. 5, are shown in Fig. 13.

### 7.1. Varied parameters

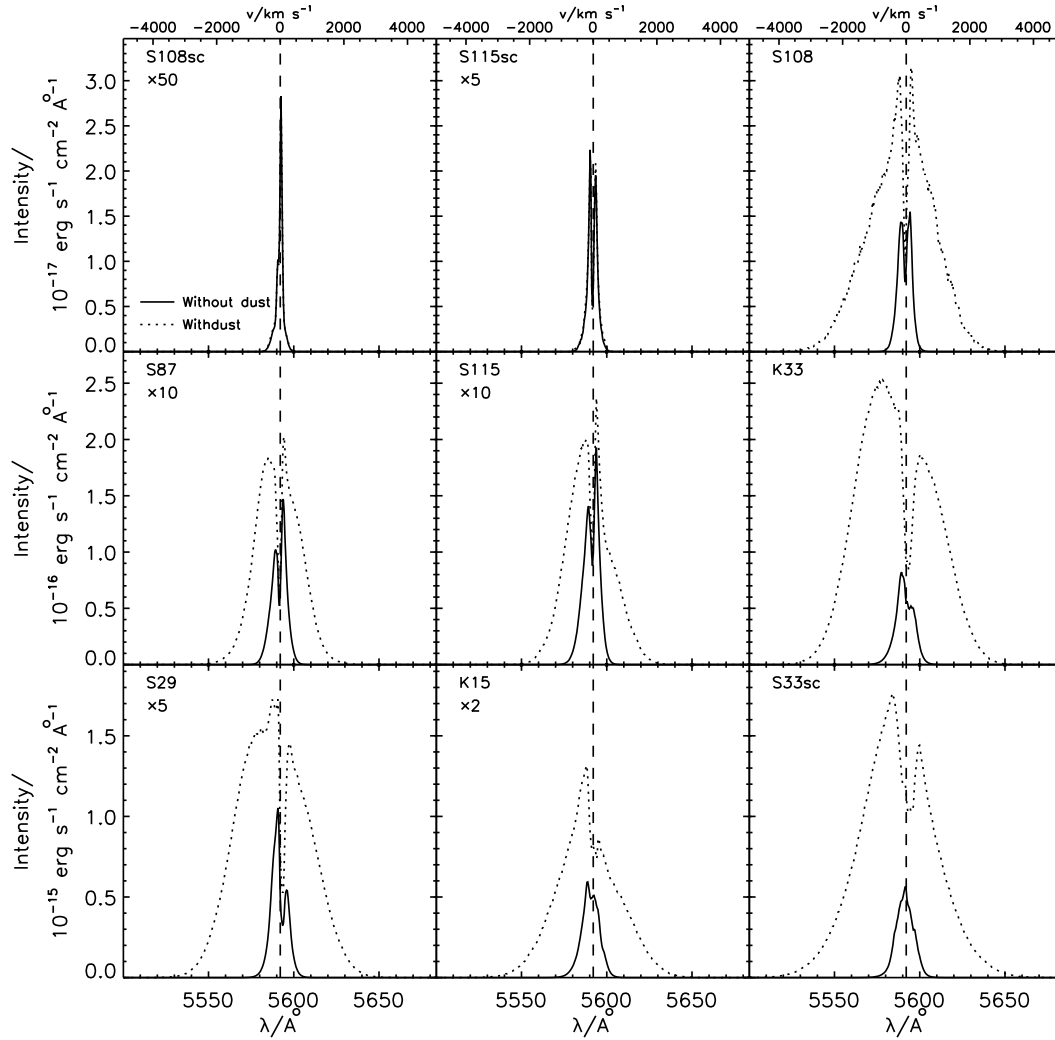


FIG. 10.— Emergent spectra of the studied galaxies, without dust (*dotted*) and with dust (*solid*), ordered after decreasing virial mass. In order to use the same ordinate axis for a given row, some intensities have been multiplied a factor indicated under the name of the galaxy. Generally, lines that are broadened by resonant scattering tend to be severely narrowed when including dust.

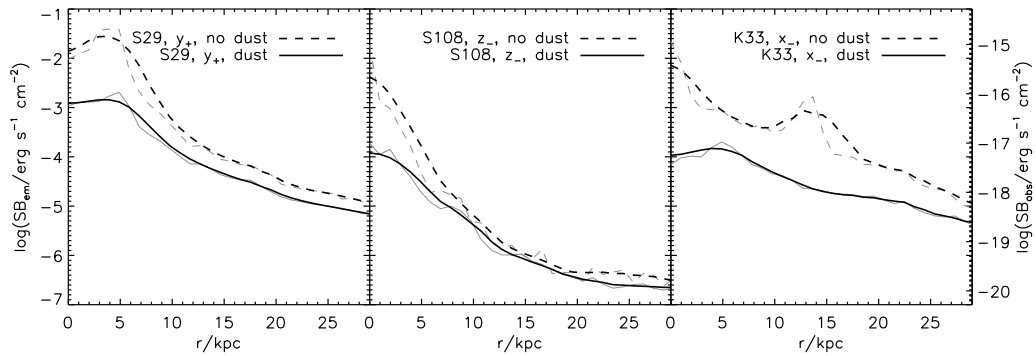


FIG. 11.— Ly $\alpha$  surface brightness (SB) profiles of three of the simulated galaxies as observed from three arbitrary directions, with (*solid*) and without (*dashed*) dust. While the intrinsic SB profiles are shown in grey, the black lines show the profiles convolved with a Gaussian kernel corresponding to a seeing of  $0''.5$ . In general, the inclusion of dust tends to “smooth out” the profiles, effectively resulting in a more extended SB profile.

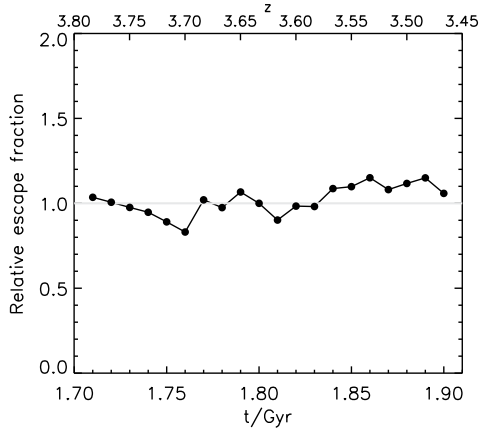


FIG. 12.— Escape fraction  $f_{\text{esc}}$  from the galaxy K15 as a function of time  $t$  over a period of 200 Myr, normalized to  $f_{\text{esc}}$  at  $t = 1.8$  Gyr. The dispersion of  $f_{\text{esc}}$  over time is quite small, indicating that the dispersion in Fig. 9 is due to galaxy-to-galaxy variations rather than the escape fractions of the individual galaxies fluctuating.

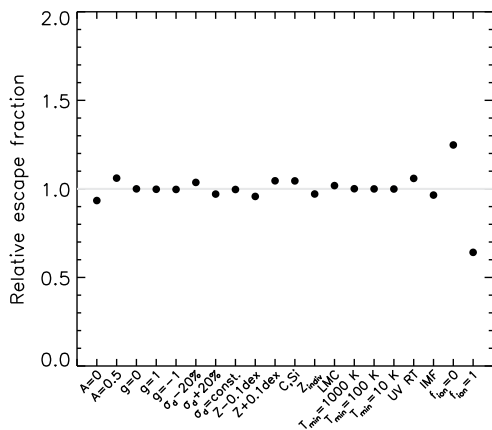


FIG. 13.— Relative escape fraction  $f_{\text{esc}}$  from the galaxy K15 as a “function” of model, i.e. simulation where all parameters but one are equal to that of the benchmark model used for the simulations in Sec. 5. See §7.1 for an explanation of abscissa labels. Except for the factor  $f_{\text{ion}}$ , the chosen benchmark model appears quite robust to varying other parameters.

*The albedo  $A$  of the dust grains.* The chosen value of 0.32 is bracketed by the values 0.5 and 0, i.e. somewhat more reflective and completely black, respectively. As expected, the higher the albedo, the higher the escape fraction, but note that even completely black dust reduces  $f_{\text{esc}}$  by less than 10%. This is because the bulk of the photons is absorbed in the very dense environments, where scattering off of one grain in many cases just postpones the absorption to another grain.

*The scattering asymmetry parameter  $g$ .* The three cases  $g = 0, 1, -1$  are tested, corresponding to isotropic scattering, total forward scattering, and total backscattering. The difference from the benchmark model value of 0.73 is virtually non-existent; the fact that most of the scatterings take place in the dense environments makes the transfer be dominated by scattering on hydrogen.

*The dust cross-section  $\sigma_d$ .* Fitzpatrick & Massa (2007) showed that the variance of the extinction curves (in the

MW, normalized to  $A_V$ ) is approximately 20% at the Ly $\alpha$  wavelength. Decreasing (increasing) the dust cross-section by this quantity increases (decreases) the escape fraction as expected, but not by more than  $\sim \pm 5\%$  percent. Also, a constant cross-section with  $\sigma_d = \sigma_d|_{x=0}$  was tested, but with no notable effect.

Likewise, a variance of *the reference metallicity  $Z$*  is present from sightline to sightline in the Magellanic Clouds, probably at least 0.1 dex. Using a smaller (larger) reference  $Z$  makes the metallicity in the simulations comparatively larger (smaller), with a larger (smaller) dust density as a result and hence a smaller (larger) escape fraction. Since the escaping photons represent different sightlines in the galaxies, it is fair to use the average  $Z$  (for the individual metals) in Eq. (5), but to investigate the sensitivity on the reference metallicity, simulations with  $Z_{\text{SMC}}$  increased (reduced) by 0.1 dex was run, resulting in a  $-5\%$  ( $+5\%$ ) change in  $f_{\text{esc}}$ .

Letting  $n_d$  scale with the metallicity of only C and Si instead of the total metallicity does not alter  $f_{\text{esc}}$  much either. This model is relevant since C and Si probably are the main constituents of dust.

Although the metallicity of the Magellanic Clouds is smaller than that of the MW, the *relative* abundances between the various elements are more or less equal. Small deviations do exist, however, but letting  $n_d$  scale with the metallicity of the individual metals does not change the results much (point labeled “ $Z_{\text{indiv}}$ ” in Fig. 13).

*Dust type.* Using an LMC extinction curve instead of SMC results in a slightly (few %) larger escape fraction, since the quantity  $\tau_d \propto n_d \sigma_d \propto \sigma_d / Z_0$  is roughly 10% lower for the LMC than for the SMC.

*The minimum temperature  $T_{\text{min}}$  of the simulations.* The cosmological simulation includes cooling of the gas to  $\sim 10^4$  K. Since the temperature affects the RT of Ly $\alpha$ , we artificially lowered the temperature of the cells with  $T \simeq 10^4$  K to  $10^3, 10^2$  (approximately the temperature of the cold neutral medium), and 10 K (approximately the temperature of a molecular cloud), to see if not including sufficient cooling could affect the results. However, as is seen in Fig. 13, the difference is insignificant.

*The ionizing UV RT scheme.* As mentioned already, implementing a more realistic UV RT scheme does not alter the outcome of the non-dusty Ly $\alpha$  RT significantly. When including dust, as seen from Fig. 13 the improved RT results in a slightly increased  $f_{\text{esc}}$ , although less than 10%. The reason is that this RT is more efficient than the “old” RT scheme at ionizing the neutral gas in the immediate vicinity of the stars and, accordingly, at lowering the dust density. However, in these regions the gas density is so high that ionization in most cases is followed by instantaneous recombination, and hence the physical state of the gas in the case of the improved RT is not altered significantly.

*The initial mass function.* Since a Salpeter IMF is more top-heavy than a Kroupa IMF, i.e. produces relatively more massive stars per stellar mass, it also yields a higher metallicity and hence a higher absorption by dust. However, the increased feedback from the massive stars serves as to counteract star formation, and these two effects more or less balances each other. The ratio of the Kroupa-to-Salpeter feedback energy is 0.617, while for the yield the ratio is 0.575 (for oxygen). The result, as is seen from Fig. 13, is only a slightly smaller escape

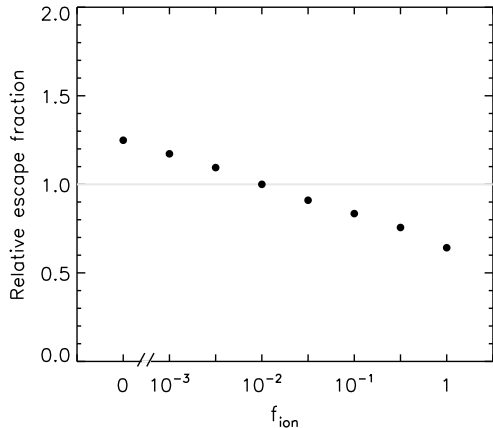


FIG. 14.— Relative variation in escape fraction  $f_{\text{esc}}$  from the galaxy K15, as a function of  $f_{\text{ion}}$ , the fraction of ionized hydrogen that contributes to the density of dust [Eq. (5)]. Note the discontinuity on the abscissa axis. Even a little dust in the ionized region can affect  $f_{\text{esc}}$  quite a lot.

fraction.

The fraction of ionized hydrogen  $f_{\text{ion}}$  contributing to the dust density. Insufficient knowledge about the dust contents of ionized gas is by far the greatest source of uncertainty in  $f_{\text{esc}}$ , as is seen in the figure. This effect is further investigated in Fig. 14, where the relative escape fraction from K15 for different values of  $f_{\text{ion}}$  is shown.

From the figure, it is seen that even a little amount of dust associated with the ionized hydrogen can affect the escape fraction quite a lot. The reason is that most of the scatterings and the absorption take place in the dense region where also the star formation is high. In these regions supernova feedback shockwaves will recurrently sweep through the ISM, heating and ionizing the medium without significantly lowering the density. For  $f_{\text{ion}} = 1$ , the calculated dust density of these regions is not affected, while for  $f_{\text{ion}} = 0$ , this effect renders the gas virtually dustless, resulting in highly porous medium with multiple possibilities for the photons of scattering their way out of the dense regions.

The resulting escape fraction of the benchmark model lies approximately midway between the two extrema and if nothing else,  $f_{\text{esc}}$  can be regarded as having an uncertainty given by the result of these extrema, i.e.  $\sim 20\%$ . Nevertheless, we believe that  $f_{\text{ion}} = 0.01$  is a realistic value, cf. the discussion in § 2.2.1.

### 7.2. Resolution dependency

The galaxies studied have been extracted from a medium resolution cosmological simulation and then re-simulated at 8 times higher resolution. To check if the resolution is sufficient to trust the results,  $f_{\text{esc}}$ -calculations were also performed at the medium resolution. The resulting SB profile and spectrum for K15 is seen in Fig. 15. The resulting escape fraction is a tiny bit lower than for the hi-res simulation, but less than 5%.

To investigate the significance of the AMR structure, we also carried out simulations progressively desolving the structure level by level. In K15, K33, and S115, the maximum level  $\mathcal{L}$  of refinement is 7, where  $\mathcal{L} = 0$  corresponds to the unrefined base grid of  $128^3$  cells. Eight cells of  $\mathcal{L} = \ell$  are desolved to  $\mathcal{L} = \ell - 1$  by taking the average

of the physical parameters. Since temperature reflects the internal energy of a body of gas, and since the combined velocity is given by momentum,  $T$  and  $\mathbf{v}_{\text{bulk}}$  are weighted by mass.

Figure 16 shows the resulting escape fractions of these three galaxies. Desolving the first few levels does not alter  $f_{\text{esc}}$  notably, indicating that the galaxies are sufficiently resolved. However, eventually we see the importance of the AMR structure: with insufficient resolution, the clumpiness of the central, luminous ISM is lost, “smoothing out” the low-density paths that facilitate escape, and consequently  $f_{\text{esc}}$  decreases. When the resolution becomes even worse, the central regions are averaged with the surrounding low-density gas, so that most of the photons are being emitted from medium dense cells, resulting in a small probability of scattering on neutral hydrogen, and hence a small probability of being absorbed by dust.

## 8. SUMMARY AND DISCUSSION

We have undertaken numerical radiative transfer calculations for Ly $\alpha$  in high-redshift galaxies including the effects of dust, with special emphasis on the fraction of photons escaping the galaxies as well as the impact on the emergent spectra. The abundance of, and the interaction probability with, dust is modeled by scaling known extinction curves to the (location-specific) metallicity of the galaxies, and destruction processes are modeled by reducing the dust density in regions where hydrogen is ionized.

The main results are listed below:

- The escape fraction of Ly $\alpha$  seems to decrease with increasing virial mass of the host galaxy. This is indicated by Fig. 9, which show that  $f_{\text{esc}}$  is close to unity for galaxies of  $M_{\text{vir}} \sim 10^9\text{--}10^{10} M_{\odot}$ , while it falls off to a few % for  $M_{\text{vir}} \sim 10^{11}\text{--}10^{12} M_{\odot}$ . This effect could be caused partly by the fact that smaller galaxies experience less total star formation, so that the total amount of metals, and hence dust, is smaller than for massive galaxies. However, since the same trend is seen for the escape of ionizing UV radiation (Razoumov & Sommer-Larsen 2009), for which dust is less important, the chief factor is likely to be feedback energy of the smaller galaxies being able to “puff up” and disorder its host to a larger degree than for massive galaxies, due to their gravitational potential being smaller.
- Although the cross-section of the dust is nearly independent of the wavelength of light over the Ly $\alpha$  line, the spectrum is affected in a highly wavelength dependent fashion: close to the line center, the escape fraction is of the order 50%, while it quickly approaches zero in the wings. Consequently, the line is severely narrowed, although its width may still reach several 100s of  $\text{km s}^{-1}$ .

The reason is that different parts of the spectrum originates in physically distinct environments of its host galaxy. The bulk of the Ly $\alpha$  photons is produced in the central, dense regions, where hot stars ionize the surrounding hydrogen which subsequently recombines, eventually resulting in  $\sim 2$  Ly $\alpha$  photons for every 3 ionizing photon. Since the optical depth of neutral hydrogen is so immense,

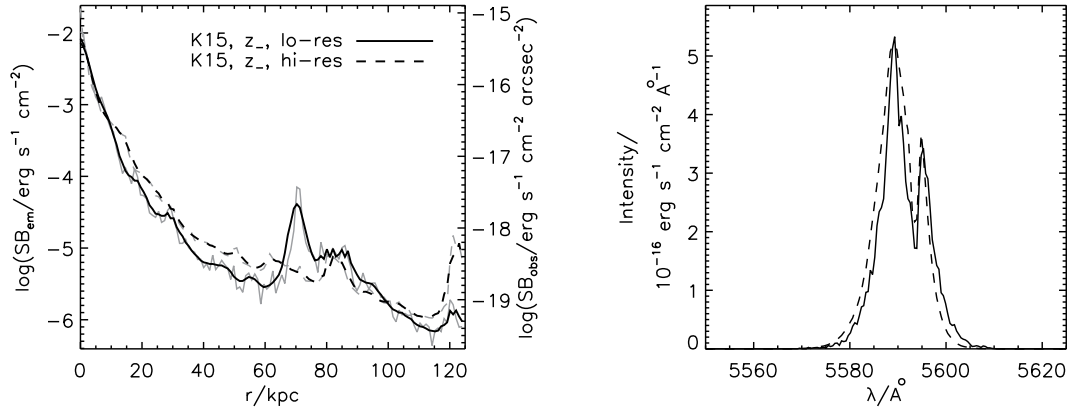


FIG. 15.— Comparison of the surface brightness profile (*left*) and emergent spectrum (*right*) of the radiation escaping the galaxy K15 when performed on galaxies simulated at low (*solid*) and high (*dashed*) resolution. Grey lines show the true profile and black lines show the profile convolved with a seeing of  $0''.5$ . While the SB in the central regions appear to agree nicely, the fact that we are comparing two different simulations make luminous regions in the outskirts appear somewhat shifted.

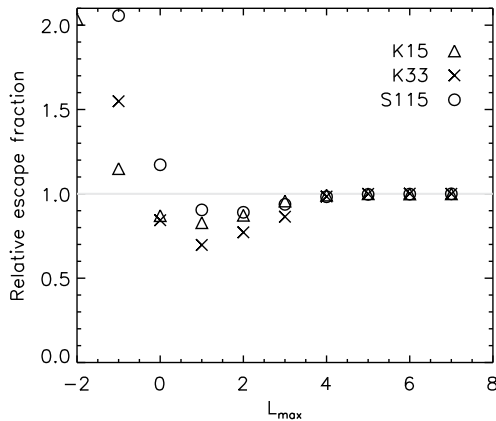


FIG. 16.— Relative escape fractions  $f_{\text{esc}}$  from the three galaxies K15, K33, and S115 as a function of the maximum level  $\mathcal{L}_{\text{max}}$  of AMR refinement.  $\mathcal{L}_{\text{max}} = 0$  corresponds to having only the  $128^3$  base grid, while  $\mathcal{L}_{\text{max}} < 0$  corresponds to desolving the base grid. For increasingly lower resolution,  $f_{\text{esc}}$  drops due to the low-density paths being smeared out with high-density regions. Eventually, however, when the resolution is so coarse that the central star- and gas-rich regions are mixed with the surrounding low-density region,  $f_{\text{esc}}$  increases rapidly.

in order to escape the photons have to diffuse in frequency to either the blue or the red side of the line center, where the cross-section falls off rapidly. Hence, the wings of the spectrum emanates from the star-forming regions, whereas the central parts to a high degree stems from the regions less populated by stars, and from gravitational cooling of infalling gas. Since the dust originates from stars, by far most of the dust is found where the wings are produced, meaning that this part of the spectrum is affected the most by the dust.

- For the same reason, the surface brightness profiles of galaxies, when observed in Ly $\alpha$ , is “smoothed out”. Without dust, the central parts of the galaxies are often very luminous compared to the outer parts, thus resulting in a central bump in the SB profile. With dust, this bump is reduced, giving

rise to an even more “flat” SB profile, which can then be interpreted as an extended SB profile when comparing to continuum bands.

Laursen & Sommer-Larsen (2007) found that even without dust, scattering effects alone can explain extended Ly $\alpha$  profiles, although the very central parts may exhibit a steeper profile. Including dust in the calculation tends to remove these central bumps and thus flatten the profile.

The obtained results ( $f_{\text{esc}}$ , SB, spectra) seem to be quite insensitive to the assumed values of various parameters characterizing the dust, such as dust albedo, scattering asymmetry, dust cross-section, extinction curve, etc. Of the studied input parameters, the only actual uncertainty comes from insufficient knowledge about the dust contents of ionized gas, but this probably *at most* introduces an error of  $\sim 20\%$ . This robustness against input parameters is convenient in the sense that we can rely on the results, but is also a nuisance since at least from Ly $\alpha$  observations, we should not expect to be able to learn much about the physical properties of the dust itself.

As discussed in the introduction, previous attempts to determine Ly $\alpha$  escape fractions have been quite divergent, ranging from a few percent to close to a hundred percent. In this work we have shown that  $f_{\text{esc}}$  may indeed vary rather much from galaxy to galaxy, and we propose a tentative evidence for a negative correlation with galactic mass. Obviously, many factors play a role in regulating  $f_{\text{esc}}$ ; in particular the age of a given galaxy will be significant, since the dust accumulates over time.

Various authors have invoked different scenarios to explain their inferred escape fractions, e.g. galactic outflows, ionized paths, multi-phase medium, and viewing angle. We find no evidence that any single of these scenarios should be dominating entirely the magnitude of  $f_{\text{esc}}$ . Rather, a mixture of gas kinematics, ISM clumpiness and ionization state, as well as viewing angle will influence the total observed Ly $\alpha$  luminosity, and hence the deduced escape fraction. The investigated galaxies exhibit both outflows and infall, but not at exceptionally high velocities, and artificially setting all velocities to zero

still allows plenty of radiation to escape (this was done for K15; the shape of the spectrum is altered, but  $f_{\text{esc}}$  still is around 0.16). Artificially erasing the clumpiness of the ISM decreases  $f_{\text{esc}}$  as expected but also in this case much radiation still escapes. The luminosity observed from different directions may vary by a factor of  $\sim 1.5$  to  $\sim 4$ . Note, however, that this factor could increase if the effect of AGN was implemented in the cosmological simulations.

We have also investigated the variation in  $f_{\text{esc}}$  over a time span of 200 Myr, and found that  $f_{\text{esc}}$  exhibits only minor fluctuations.

We have focused on the escape of Ly $\alpha$  photons from galaxies, and did not take into account any absorption/scattering in the IGM. At  $z = 3.6$ , the Universe is expected to be highly ionized, and thus most of the radiation should be able to propagate freely once the

host galaxy has been escaped. Preliminary RT calculations using MOCALATA on cosmological volumes indicate that, on average, approximately 80% of all of the radiation blueward of the Ly $\alpha$  line center should be transmitted, while the Universe is effectively transparent to radiation redward of the line center (Laursen et al., in prep.).

We are grateful to Alex O. Razoumov for calculating the realistic temperature and ionization state of the gas, and to Kim K. Nilsson and Johan P. U. Fynbo for giving useful comments on the draft. The simulations were performed on the facilities provided by the Danish Center for Scientific Computing. The Dark Cosmology Centre is funded by the Danish National Research Foundation.

## APPENDIX

### ACCELERATION SCHEMES

#### *Core-skipping scheme*

For a photon with frequency close to the line center, the opacity of the gas is so high that the photon does not diffuse significantly in space. In order to accelerate to execution time of the code, these scatterings can be skipped by drawing the velocity of the scattering atom not from a pure Gaussian but from a Gaussian where the inner part is truncated, such that higher velocities and hence large frequency shifts are favored. This acceleration scheme is invoked whenever  $|x| \leq x_{\text{crit}}$ , where  $x_{\text{crit}}$  varies according to the physical conditions in the cell (for a detailed explanation, see Laursen et al. 2009).

With a dusty medium, we must investigate the possibility that the photon would have been destroyed, had we *not* used this acceleration scheme, i.e. the probability  $P_{\text{abs}}(x_{\text{crit}})$  of absorption for a photon initially in the core, before escaping the frequency interval  $[-x_{\text{crit}}, x_{\text{crit}}]$ . Ultimately, we will determine this probability numerically, but to interpret the result, we will first investigate the scenario analytically. In the following calculation, factors of order unity will be omitted.

The probability per interaction that a photon with frequency  $x$  be absorbed is

$$p_{\text{abs}}(x) = \frac{\tau_{\text{a}}}{\tau_{\text{d}} + \tau_x} \sim \frac{1}{1 + \phi(x)\tau_0/\tau_{\text{a}}}, \quad (\text{A1})$$

since  $\tau_{\text{a}} \sim \tau_{\text{d}}$  and  $\tau_x \sim \phi(x)\tau_0$ . Here,  $\tau_{\text{a,d},x,0}$  corresponds to the optical depth of this particular part of the journey. The number  $dN(x)$  of scatterings taking place when the frequency of the photon is close to  $x$  is

$$dN(x) = N_{\text{tot}}\phi(x)dx, \quad (\text{A2})$$

where  $N_{\text{tot}}$  is the total number of scatterings before the photon exits  $[-x_{\text{crit}}, x_{\text{crit}}]$ , i.e. the total number of scatterings skipped. Here we have assumed *complete redistribution* of the frequency, i.e. there is no correlation between the frequency of the photon before and after the scattering event. This is a fair approximation in the core (Unno 1952b; Jefferies & White 1960). However, Osterbrock (1962) showed that once the photon is in the wing, it has a tendency to stay there, only slowly drifting toward the line center with a mean shift per scattering  $\langle \Delta x \rangle = -1/|x|$ .

For the purpose of the current calculation, the Voigt profile is approximated by a Gaussian in the core and a power law in the wing, such that

$$\phi(x) \sim \begin{cases} e^{-x^2} & \text{for } x < x_{\text{cw}} \\ \frac{a}{x^2} & \text{for } x \geq x_{\text{cw}}, \end{cases} \quad (\text{A3})$$

where  $x_{\text{cw}}$  marks the value of  $x$  at the transition from core to wing (Eq. (15) in Laursen et al. 2009).

At each scattering, the probability of escaping the region confined by  $x_{\text{crit}}$  is

$$\begin{aligned} p_{\text{esc}}(x_{\text{crit}}) &= 2 \int_{x_{\text{crit}}}^{\infty} \phi(x)dx \\ &\sim \begin{cases} \text{erfc } x_{\text{crit}} & \text{for } x_{\text{crit}} < x_{\text{cw}} \\ \frac{a}{x_{\text{crit}}} & \text{for } x_{\text{crit}} \geq x_{\text{cw}}, \end{cases} \end{aligned} \quad (\text{A4})$$

where erfc is the complimentary error function.

Using Eq. (A2), the total probability of being absorbed can be calculated as

$$P_{\text{abs}}(x_{\text{crit}}) = \int_0^{x_{\text{crit}}} p_{\text{abs}}(x)dN(x) = N_{\text{tot}} \int_0^{x_{\text{crit}}} p_{\text{abs}}(x)\phi(x)dx(x). \quad (\text{A5})$$



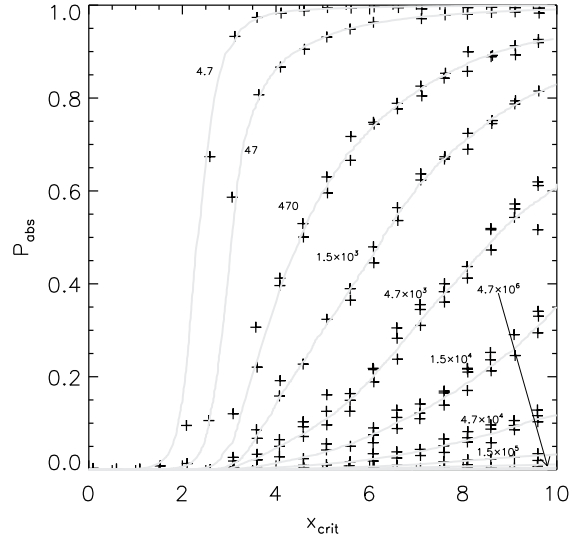


FIG. 17.— Probability of absorption  $P_{\text{abs}}$  before escaping the region of the line confined by the value  $x_{\text{crit}}$ , for a series of different values of  $a\tau_0/\tau_a$  (labeled at the corresponding lines).

The total number of scatterings before escape if the photon is not absorbed is  $N_{\text{tot}} \sim 1/p_{\text{esc}}$ . For  $x_{\text{crit}} < x_{\text{cw}}$ , from Eqs. (A1) and (A4), Eq. (A5) then evaluates to

$$P_{\text{abs}}(x_{\text{crit}}) \sim \frac{1}{\text{erfc}x_{\text{crit}}} \int_0^{x_{\text{crit}}} \frac{dx}{e^{x^2} + \tau_0/\tau_a}. \quad (\text{A6})$$

The exponential integral and the factor  $1/\text{erfc}x_{\text{crit}}$  is of the same order, but since the factor  $\tau_0/\tau_a$  is of the order  $10^8 Z/Z_\odot$ , Eq. (A6) will usually be negligible.

In the case of  $x_{\text{crit}} \geq x_{\text{cw}}$ ,

$$P_{\text{abs}}(x_{\text{crit}}) \sim \int_0^{x_{\text{crit}}} \frac{dx}{a/\phi(x) + a\tau_0/\tau_a}. \quad (\text{A7})$$

This integral can be evaluated separately for the intervals  $[0, x_{\text{cw}}[$  and  $[x_{\text{cw}}, x_{\text{crit}}]$ . For the first, the result is usually negligible, as in the case with Eq. (A6). The second integral yields

$$P_{\text{abs}}(x_{\text{crit}}) \sim \frac{1}{\mathfrak{t}} \left( \tan^{-1} \frac{x_{\text{crit}}}{\mathfrak{t}} - \tan^{-1} \frac{x_{\text{cw}}}{\mathfrak{t}} \right), \quad (\text{A8})$$

where

$$\mathfrak{t} \equiv (a\tau_0/\tau_a)^{1/2}. \quad (\text{A9})$$

For  $x_{\text{crit}} \geq x_{\text{cw}}$ , the assumption of complete redistribution becomes very inaccurate, as the photon spends considerably more time in the wings, with a larger probability of being destroyed. However, Eqs. (A8) and (A9) reveals a signature of the behavior of  $P_{\text{abs}}(x_{\text{crit}})$ , viz. that it has a “ $\tan^{-1}$ -ish” shape, and that it scales not with the individual parameters  $a$ ,  $\tau_0$ , and  $\tau_a$ , but with their interrelationship as given by the parameter  $\mathfrak{t}$ . To know exactly the probability of absorption, a series of Monte Carlo simulations were carried out for a grid of different temperatures, gas densities, and dust densities. The results, which are stored as a look-up table, are shown in Fig. 17. Indeed, the same fit applies approximately to different  $T$ ,  $n_{\text{HI}}$ , and  $n_{\text{d}}$  giving equal values of  $\mathfrak{t}$ .

Whenever the acceleration scheme is applied, a bilinear interpolation over  $\log(\mathfrak{t})$  and  $x_{\text{crit}}$  determines the appropriate value of  $P_{\text{abs}}$ . A univariate is then drawn and compared to  $P_{\text{abs}}$ , thus determining if the photon is absorbed or allowed to continue its journey. Note that under most physically realistic conditions, only low values of  $P_{\text{abs}}$  are actually met. However, when invoking the acceleration scheme many times, the probability of absorption may become significant.

#### *Semi-analytical scheme*

In very dense regions, defined in the simulations as cells with  $a\tau_0 > 2000$ , the code can be further accelerated by calculating analytically the characteristics of a photon escaping such a region. Laursen et al. (2009) found that the spectrum of photons escaping a sufficiently dense cube is characterized by the analytical solution for the spectrum from an equivalent “slab” of gas found by Harrington (1973), with the exception that the independent variable  $a\tau_0$  (where  $\tau_0$  is measured from the center to the face of the cube) be replaced by  $\eta a\tau_0$ , where  $\eta = 0.71$  is a fitting parameter (for a detailed explanation, see Laursen et al. 2009).

With the inclusion of dust, we must calculate the possibility of the photon being absorbed in such a cube. From the above, we might expect that replacing  $a\tau_0$  by  $\eta a\tau_0$  and  $\tau_a$  by  $\eta\tau_a$  in the slab-relevant equation for the escape fraction

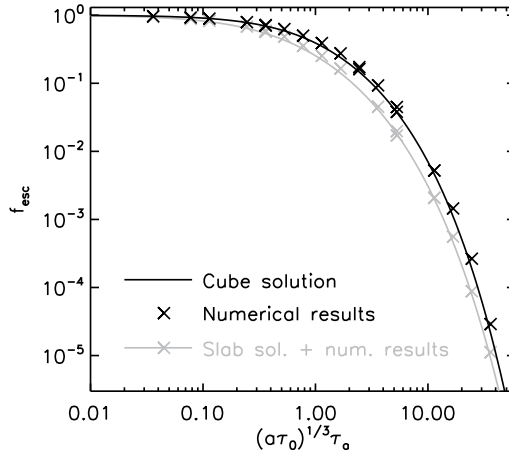


FIG. 18.— Escape fractions (*black crosses*) of photons emitted from the center of a cube of damping parameter  $a$ , line center optical depth  $\tau_0$ , and dust absorption optical depth  $\tau_a$ , measured from the center to the face, compared to the analytical solution (solid black) given by Eq. (A10). For comparison, the equivalent results for the slab (grey; the same as in Fig. 2) are also displayed.

[Eq. (11)] yields the relevant solution. In fact, even better fits can be achieved by also replacing the square root by an exponentiation to the power of 0.55. That is, every time the semi-analytical acceleration scheme is invoked, a univariate is drawn and compared to the quantity

$$f_{\text{esc}} = \frac{1}{\cosh\left(\zeta' \left[\eta^{4/3} (a\tau_0)^{1/3} (1-A)\tau_d\right]^{0.55}\right)}, \quad (\text{A10})$$

determining whether or not the photon should continue its journey.

Figure 18 shows the calculated escape fractions from a number of cubes of different physical properties. The tests performed in §4 and many of the results of §5 were performed both with and without this acceleration scheme, all agreeing to a few percent within statistical errors.

#### Luminosity boosting scheme

Since the vast majority of the photons are emitted within a relatively small volume of the total computational domain, many photons are needed to reach good statistics in the outer regions. In order to reach convergence faster, the probability of emitting photons from low-luminosity cells can be artificially boosted by some factor  $1/w > 1$ , later corrected for by letting the emitted photon only contribute with a weight  $w$  to statistics (spectra, SB profiles, escape fractions).

This factor is calculated for the  $i$ 'th cell as

$$w_i = 10^{\log(L_i/L_{\text{max}})/b}, \quad (\text{A11})$$

where  $L_i$  is the original luminosity of the cell,  $L_{\text{max}}$  is the luminosity of the most luminous cell (not to be confused with  $\mathcal{L}_{\text{max}}$ ), and  $b$  is a “boost buffer” factor that determines the magnitude of the boost; for  $b = 1$ , all cells will have an equal probability of emitting a photon while for  $b \rightarrow \infty$  the probability approaches to original probability.

The optimal value of  $b$  depends on the quantity and physical region of interest. Since photons are absorbed primarily in the central regions,  $f_{\text{esc}}$ -calculation will usually converge fastest using  $b \rightarrow \infty$ , and since after all most photons are received from this region as well, the same counts for the spatially integrated spectrum. If one wishes to investigate the SB or the spectrum of the outer regions,  $b$  should not simply be set equal to unity, however, since a significant fraction of the photons received from here are photons originating in the central parts and later being scattered in the direction of the observer. In this case, faster convergence can be reached with  $b \sim 1.5$  to a few tens.

#### REFERENCES

- Aannestad, P. A. & Emery, R. J. 2001, *A&A*, 376, 1040  
Aguirre, A., Hernquist, L., Schaye, J., Katz, N., Weinberg, D. H., Gardner, J. 2001, *ApJ*, 561, 521  
Atek, H., Kunth, D., Hayes, M., Östlin, G., Mas-Hesse, J. M. 2008, *A&A*, 488, 491  
Bianchi, L., Clayton, G. C., Bohlin, R. C., Hutchings, J. B., & Massey, P. 1996, *ApJ*, 471, 203  
Bohlin, R. C., Savage, B. D. & Drake, J. F. 1978, *ApJ*, 224, 132  
Bouchet, P. et al. 2006, *ApJ*, 650, 212  
Burgh, E. B., McCandliss, S. R., & Feldman, P. D. 2002, *ApJ*, 575, 240  
Calzetti, D., Bohlin, R. C., Gordon, K. D., Witt, A. N., & Bianchi, L. 1995 *ApJ*, 446, 97  
Chelouche, D., Koester, B. P., Bowen, D. V. 2007, *ApJ*, 671, 97  
Chini, R., Krügel, E., & Kreysa, E. 1986, *A&A*, 167, 315  
Contini, M. 2004, *A&A*, 422, 591  
Contini, M. & Contini, T. 2003, *MNRAS*, 342, 299  
Coppin, K., et al. 2009 (arXiv:0902.4464)  
Davé, R., Finlator, K., & Oppenheimer, B. D. 2006, *MNRAS*, 370, 273

- Dayal, P., Ferrara, A., Saro, A., Salvaterra, R., Borgani, S., & Tornatore, L. 2009 (arXiv:0907.0337)
- Draine, B. T. 1988, *AJ*, 333, 848
- Draine, B. T. & Salpeter, E. E. 1979, *ApJ*, 231, 438
- Draine, B. T. & Salpeter, E. E. 1979, *ApJ*, 231, 77
- Dunne, L., Morgan, H., Eales, S., Ivison, R., Edmunds, M. 2004, *New Astr. Rev.*, 48, 611
- Elíasdóttir, Á. et al. 2009 *ApJ*, 697, 1725
- Ellison, S. L. 2006, *MNRAS*, 372, 38
- Ferland, G. J., Korista, K. T., Verner, D. A., et al. 1998, *PASP*, 110, 761
- Finkelstein, S. L., Rhoads, J. E., Malhotra, S., Grogin, N., Wang, J. 2008 *ApJ*, 678, 655
- Fitzpatrick, E. L. & Massa, D. 2007, *ApJ*, 663, 320
- Fynbo, J. P. U., Møller, P., & Thomsen, B. 2001, *A&A*, 374, 443
- Fynbo, J. P. U., Ledoux, C., Møller, P., Thomsen, B. & Burud, I. 2003, *A&A*, 407, 147
- Gawiser et al. 2006, *ApJS*, 162, 1
- Gawiser et al. 2006, *ApJ*, 642, 13
- Giard, M., Montier, L., Pointecouteau, E., & Simmat, E. 2008, *A&A*, 490, 547
- Gnedin, N. Y. Kravtsov, A. V., & Chien, H.-W. 2004, *ApJ*, 672, 765
- Gordon, K. D., Clayton, G. C., Misselt, K. A., Landolt, A. U., & Wolff, M. J. 2003, *ApJ*, 594, 279
- Greenberg, J. M. 1976, *Ap&SS*, 39, 9
- Gronwall et al. 2007, *ApJ*, 667, 79
- Haardt, F. & Madau, P. 1996, *ApJ*, 461, 20
- Hansen, M. & Oh, S. P. 2006, *MNRAS*, 367, 979
- Harper, D. A. & Low, F. J. 1971, *ApJ*, 165, 9
- Harrington, J. P. 1973, *MNRAS*, 162, 43
- Heney L. G. & Greenstein J. L. 1941, *AJ*, 93, 70
- Höfner, S. & Andersen, A. C. 2007, *A&A*, 465, 39
- Jakobsson, P. et al. 2004, *A&A*, 427, 785
- Jefferies, J. T. & White, O. R. 1960, *ApJ*, 132, 767
- Junkkarinen, V. T., Cohen, D., Beaver, E. A., Burbidge, E. M., Lyons, R. W., & Madejski, G. 2004, *ApJ*, 614, 658
- Keller, S. C. & Wood, P. R., 2006 *ApJ*, 642, 834
- Kobayashi, M. A. R., Totani, T., & Nagashima, M. 2007, *ApJ*, 670, 919
- Kottak et al. 2009 (arXiv:0904.3737)
- Kroupa, P. 1998, *MNRAS*, 298, 231
- Kunth, D., Mas-Hesse, J. M., Terlevich, E., Terlevich, R., Lequeux, J., & Fall, S. M. 1998, *A&A*, 334, 11
- Laursen, P., Razoumov, A. O., & Sommer-Larsen, J. 2009, *ApJ*, 696, 853
- Laursen, P. & Sommer-Larsen, J. 2007, *ApJ*, 657, L69
- Le Delliou, M., Lacey, C. Baugh, C. M., Guiderdoni, B., Bacon, R., Courtois, H., Sousbie, T., & Morris, S. L. 2005, *MNRAS*, 357, 11
- Le Delliou, M.; Lacey, C. G., Baugh, C. M., & Morris, S. L. 2006, *MNRAS*, 365, L712
- Li, A. & Draine, B. T. 2001, *ApJ*, 554, 778
- Lillie, C. F. & Witt, A. N. 1976, *ApJ*, 208, 64
- Mas-Hesse, J. M., Kunth, D., Tenorio-Tagle, G., et al. 2003, *ApJ*, 598, 858
- Massa D. & Fitzpatrick E. L., 1986, *ApJS*, 60, 305
- Mattis, J. S., Rumpl, W., & Nordsieck, K. H. 1977, *ApJ*, 217, 425
- Mattsson, L., Wahlin, R., Hfner, S., & Eriksson, K. 2008, *A&A*, 484, 5
- Malhotra, S. & Rhoads, J. E. 2002, *ApJ*, 565, 71
- Montier, L. A. & Giard, M. 2004, *A&A*, 417, 401
- Morton, T. D., Slane, P., Borkowski, K. J., Reynolds, S. P., Helfand, D. J., Gaensler, B. M., Hughes, J. P. 2007, *ApJ*, 667, 219
- Møller, P. & Warren, S. J. 1998, *MNRAS*, 299, 611
- Nagamine, K., Ouchi, M., Springel, V., Hernquist, L. 2008 (arXiv:0802.0228)
- Nandy, K., Morgan, D. H., Willis, A. J., Wilson, R., & Gondhalekar, P. M. 1981, *MNRAS*, 196, 955
- Neufeld, D. 1990, *ApJ*, 350, 216
- Neufeld, D. 1991, *ApJ*, 370, L85
- Nilsson, K. K., Fynbo, J. P. U., Møller, P., Sommer-Larsen, J. & Ledoux, C. 2006, *A&A*, 452, 23
- Nilsson, K. K., Orsi, A., Lacey C. G., Baugh, C. M., & Thommes, E. 2007, *A&A*, 474, 385
- Nilsson, K. K., Tapken, C., Møller, P., Freudling, W., Fynbo, J. P. U., Meisenheimer, K., Laursen, P., Östlin, G. 2009, *A&A*, 498, 13
- Osterbrock, D. E. 1962, *ApJ*, 135, 195
- Ouchi, M. et al. 2008 *ApJS*, 176, 301
- Pei, Y. C. 1992, *ApJ*, 395, 130
- Pei, Y., Fall, M. & Hauser, M. 1998, *ApJ*, 522, 604
- Pettini, M., King, D., Smith, L., & Hunstead, R. 1997, *ApJ*, 478, 536
- Prevot, M. L., Lequeux, J., Prevot, L., Maurice, E., & Rocca-Volmerange, B. 1984, *A&A*, 132, 389
- Purcell, E. M. & Pennypacker, C. R. 1973, *AJ*, 186, 705
- Razoumov, A. O. & Sommer-Larsen, J. 2006, *ApJ*, , 651, 81
- Razoumov, A. O. & Sommer-Larsen, J. 2007, *ApJ*, , 668, 674
- Razoumov, A. O. & Sommer-Larsen, J. 2009, (arXiv:0903.2045)
- Rhoads, J. E., et al. 2003, *AJ*, 125, 1006
- Russell, S. C. & Dopita, M. A. 1992 *ApJ*, 384, 508
- Salpeter, E. 1955, *ApJ*, 121, 161
- Santos, M. R., Ellis, R. S., Kneib, J.-P., Richard, J., & Kuijken, K. 2004, *ApJ*, 606, 683
- Savaglio, S., Fall, M. S. & Fiore, F. 2003, *ApJ*, 585, 638
- Schiminovich, D., Friedman, P. G., Martin, C., & Morrissey, P. F. 2001, *ApJ*, 563, 161
- Shimasaku, K., et al. 2006, *PASJ*, 58, 313
- Smith, C. H. 1999, *MNRAS*, 303, 367
- Sommer-Larsen, J., Götz, M., & Portinari, L. 2003, *ApJ*, 596, 47
- Sommer-Larsen, J. 2006, *ApJ*, 644, L1
- Srianand, R., Gupta, N., Petitjean, P., Noterdaeme, P., & Saikia, D. J. 2008, *MNRAS*, 391, 69
- Stickel, M., Klaas, U., Lemke, D., & Mattila, K. 2002, *A&A*, 383, 367
- Stratta, G., Maiolino, R., Fiore, F., & D'Elia, V. 2007, *ApJ*, 661, 9
- Tenorio-Tagle, G., Silich, S. A., Kunth, D., Terlevich, E., & Terlevich, R. 1999, *MNRAS*, 309, 332
- Unno, W. 1952, *PASJ*, 4, 100
- Vila-Costas, M. B. & Edmunds, M. G. 1993, *MNRAS*, 265, 199
- Weingartner, J. C. & Draine, B. T. 2001, *ApJ*, 548, 296
- Welty, D. E., Frisch, P. C., Sonneborn, G., & York, D. G. 1999, *ApJ*, 512, 636
- Welty, D. E., Lauroesch, J. T., Blades, J. C., Hobbs, L. M., & York, D. G. 1997, *ApJ*, 489, 672
- Witt, A. N. & Oliveri, M. V. 1990, *AJ*, 99, 888
- Xilouris, E., Alton, P., Alikakos, J., Xilouris, K., Boumis, P., & Goudis, C. 2006, *ApJ*, 651, 107
- Östlin, G., Hayes, M., Kunth, D., Mas-Hesse, J. M., Leitherer, C., Petrosian, A., Atek, H. 2008, (arXiv:0803.1174)